

# Adaptive local surface refinement based on LR NURBS and its application to contact

Christopher Zimmermann, Roger A. Sauer<sup>1</sup>

*Aachen Institute for Advanced Study in Computational Engineering Science (AICES),  
RWTH Aachen University, Templergraben 55, 52062 Aachen, Germany*

## Abstract

A novel adaptive local surface refinement technique based on *Locally Refined Non-Uniform Rational B-Splines* (LR NURBS) is presented. LR NURBS can model complex geometries exactly and are the rational extension of LR B-splines. The local representation of the parameter space overcomes the drawback of non-existent local refinement in standard NURBS-based isogeometric analysis. For a convenient embedding into a general finite element code the Bézier extraction operator for LR NURBS is formulated. A technique is presented that indicates the domain for refinement. This technique is automatically controlled and allows a robust adaptive local refinement and coarsening of LR NURBS discretizations.

In this work, LR NURBS are applied to contact computations of 3D solids and membranes. The entire membrane surface is discretized by LR NURBS, and their simulation results are compared to classical uniform NURBS discretizations. For the solids LR NURBS-enriched finite elements are used to discretize the contact surfaces with LR NURBS finite elements while the rest of the body is discretized by linear Lagrange finite elements. Various numerical examples are shown, and they demonstrate the benefit of using LR NURBS discretizations: Compared to uniform refinement, LR NURBS can achieve high accuracy at much lower computational cost.

**Keywords:** Adaptive local refinement, coarsening, isogeometric analysis, LR NURBS, LR B-splines, computational contact

## 1 Introduction

A wide range of engineering applications that are governed by local surface effects necessitate an accurate surface description. An example are contact problems. In most cases those are only solvable by numerical methods due to their strong nonlinear behavior. For this issue, isogeometric finite element discretizations are considered that offer in general at least  $C^1$ -continuity across element boundaries. Standard NURBS based discretizations lack local refinement but their ability to discretize complex geometries exactly makes them powerful. A new approach for adaptive local surface refinement of NURBS is presented. The presented technique is based on the concept of Locally Refined B-Splines (LR B-Splines) which overcomes the drawback of non-existent local refinement. This formulation is extended to Locally Refined NURBS (LR NURBS) to combine the advantages of local refinement and the ability of modeling complex geometries exactly. To allow a convenient embedding of LR NURBS into a finite element code the Bézier extraction operator for LR NURBS elements is formulated. It is shown that the presented technique leads to high accuracy in the numerical results while decreasing the computational costs in comparison to uniformly discretized models.

Isogeometric Analysis (IGA) was developed by [Hughes et al. \(2005\)](#) and the work of [Cottrell et al. \(2009\)](#) summarizes the concept of IGA in a suitable way. LR B-splines were introduced by [Dokken et al. \(2013\)](#) and further worked on by [Bressan \(2013\)](#) and [Johannessen et al. \(2014\)](#). The LR B-splines

---

<sup>1</sup>corresponding author, email: sauer@aices.rwth-aachen.de

are related to hierarchical B-splines that are introduced by [Forsey and Bartels \(1988\)](#). In contrast to hierarchical B-splines the LR B-splines assure less maximum overlap of the basis functions in the locally refined meshes and a better sparsity pattern. With an LR B-spline description new possibilities are achieved of how the computational mesh can be generated. This makes them interesting in many fields of engineering. In the works of [Nørtoft and Dokken \(2014\)](#) and [Johannessen et al. \(2015\)](#) the LR B-splines are successfully applied to the computation of Navier-Stokes flows.

T-splines were introduced by [Sederberg et al. \(2003\)](#) as an approach to discretize surfaces more efficiently than hierarchical B-splines. The refinement by LR B-splines is directly performed in the parameter domain that reflects the piecewise polynomial structure which is more convenient than the multiple vertex grids of T-splines. [Borden et al. \(2011\)](#) introduced the Bézier extraction operator which allows a suitable embedding of isogeometric analysis into existing finite element code. The work of [Scott et al. \(2011\)](#) introduces their extension to T-splines which offers a local representation of the Bézier extraction operator.

The presented numerical examples in this work are performed on membrane surfaces and solids. A computational formulation for nonlinear membrane surfaces is presented in [Sauer et al. \(2014\)](#). The theory is formulated in curvilinear coordinated considering isogeometric finite elements. The works on nonlinear membranes go back to [Oden and Sato \(1967\)](#). In general, membranes are a special case of shell surface structures that go back to the work of [Simo and Fox \(1989\)](#) and [Simo et al. \(1990\)](#). Shell formulations in the framework of isogeometric analysis have been proposed in [Kiendl et al. \(2009\)](#), [Benson et al. \(2011\)](#), [Nguyen et al. \(2014\)](#), [Sauer and Duong \(2015\)](#), [Duong et al. \(2016\)](#) and [Roohbakhshan and Sauer \(2016\)](#). In this work we present a novel technique for adaptive local surface refinement and coarsening that

- considers the extension of LR B-spline finite elements to LR NURBS finite elements
- uses a local formulation of the Bézier extraction operator
- is automatically controlled by a proposed technique
- is extended to LR NURBS-enriched finite elements for solids in 3D
- is applied to frictionless and frictional contact.

A summary of nonlinear continuum mechanics and frictional contact is presented in [Laursen \(2002\)](#) and [Wriggers \(2006\)](#). A computational formulation for 3D friction is presented in [Sauer and De Lorenzis \(2013\)](#) and [Sauer and De Lorenzis \(2015\)](#). Works on contact in the framework of IGA can be found in [De Lorenzis et al. \(2011\)](#), [Lu \(2011\)](#), [De Lorenzis et al. \(2012\)](#) and [Temizer et al. \(2012\)](#). In the work of [Temizer and Hesch \(2016\)](#) hierarchical NURBS discretizations are used that allow local refinement in the context of frictionless contact.

The linear independence of LR B-spline and LR NURBS discretizations in 3D is not proven yet. For this issue, isogeometrically enriched finite elements are used for to discretize solids in 3D in the context of contact computations. A local finite element enrichment technique for frictionless contact is presented in [Corbett and Sauer \(2014\)](#) and for frictional contact in [Corbett and Sauer \(2015\)](#). This combines the high accuracy which is achieved by isogeometric analysis and the efficiency of standard finite elements. This formulation is adapted for LR NURBS-enrichment to gain the possibility of local refinement.

In [Sec. 2.1](#) a brief summary of the nonlinear finite element formulation for membrane surfaces and solids is given. A short introduction to computational contact mechanics follows in [Sec. 2.2](#). The fundamentals of LR B-splines are presented in [Sec. 2.3](#). The geometric modeling using LR NURBS and the formulation of the Bézier extraction operator is presented in [Sec. 3](#). The technique of adaptive local refinement and coarsening using LR NURBS discretizations is presented in [Sec. 4](#). Numerical results are shown in [Sec. 5](#). The performance of LR NURBS within the proposed local refinement technique is compared to uniform meshes using NURBS discretizations. A conclusion is given in [Sec. 7](#).

## 2 Preliminaries

In this section, an overview of the fundamental mathematical formulations are presented that are used for the numerical examples in Sec. 5. A general finite element formulation for membrane surfaces and solids in the context of contact computations is discussed in Sec. 2.1 and Sec. 2.2. The fundamentals of LR B-splines are given in Sec. 2.3.

### 2.1 Finite element formulation

The finite element formulation for nonlinear membrane surfaces and solids in 3D is similar. Their governing equations (e.g. equilibrium) are different but obtaining their discretized weak form follows the same finite element approach. The weak form of a system for quasi-static contact is described by

$$\sum_{k=I}^{II} [\delta\Pi_{\text{int } k} - \delta\Pi_{c k} - \delta\Pi_{\text{ext } k}] = 0, \quad (2.1)$$

considering two objects ( $k = I, II$ ). This describes the equilibrium between the internal virtual work  $\delta\Pi_{\text{int } k}$ , the virtual contact work  $\delta\Pi_{c k}$  and the external virtual work for that in our examples  $\delta\Pi_{\text{ext } k} = 0$  holds. The mathematical formulation for nonlinear membrane surfaces in  $\mathbb{R}^3$  in the framework of curvilinear coordinates is taken from Sauer et al. (2014). A general constitutive setting and finite element formulation for solids in  $\mathbb{R}^3$  can be found in Wriggers (2008). The internal virtual work can be expressed for membrane surfaces  $\mathcal{S}_k$  in  $\mathbb{R}^3$  and solids  $\mathcal{B}_k$  in  $\mathbb{R}^3$  as

$$\delta\Pi_{\text{int } k} = \begin{cases} \int_{\mathcal{S}_k} \delta\varphi_{;\alpha k} \cdot \sigma_k^{\alpha\beta} \mathbf{a}_{\beta k} da_k, & \forall \delta\varphi_k \in \mathcal{V}_k, \quad \text{for } \mathcal{S}_k, \\ \int_{\mathcal{B}_k} \text{grad}(\delta\varphi_k) : \boldsymbol{\sigma}_k dv_k, & \forall \delta\varphi_k \in \mathcal{V}_k, \quad \text{for } \mathcal{B}_k. \end{cases} \quad (2.2)$$

Here,  $\sigma^{\alpha\beta}$  are the contra-variant components of the Cauchy stress tensor  $\boldsymbol{\sigma}$  with  $\alpha = 1, 2$  and  $\beta = 1, 2$ . The co-variant derivative of the virtual displacement field is denoted by  $\delta\varphi_{;\alpha}$  and  $\mathbf{a}_\alpha$  are the co-variant tangent vectors. The virtual contact work is expressed for the contact surfaces  $\Gamma_{c k}$  as

$$\delta\Pi_{c k} = \int_{\Gamma_{c k}} \delta\varphi_k \cdot \mathbf{t}_{c k} da_k, \quad \forall \delta\varphi_k \in \mathcal{V}_k, \quad (2.3)$$

where  $\mathbf{t}_{c k}$  denotes the contact traction on the surface  $\Gamma_{c k}$ . The system (2.1) is solved for the unknown deformation field  $\varphi_k \in \mathcal{V}_k$ , with  $\mathcal{V}_k$  as a suitable space of kinematically admissible variations. The membranes are discretized into a set of surface elements  $\Gamma_k^e$  and a set of surface contact elements  $\Gamma_{c k}^e$  such that  $\mathcal{S}_k \approx \mathcal{S}_k^h = \bigcup_e \Gamma_k^e$  and  $\Gamma_{c k} \approx \Gamma_{c k}^h = \bigcup_e \Gamma_{c k}^e$ , respectively. Similarly, the solids are discretized into a set of volume elements  $\Omega_k^e$  and a set of surface contact elements  $\Gamma_{c k}^e$  such that  $\mathcal{B}_k \approx \mathcal{B}_k^h = \bigcup_e \Omega_k^e$  and  $\Gamma_{c k} \approx \Gamma_{c k}^h = \bigcup_e \Gamma_{c k}^e$ , respectively. The superscript  $h$  denotes the approximated discrete setting. With a set of  $n^e$  basis functions  $\mathbf{N} = [N_1 \mathbf{I}, \dots, N_{n^e} \mathbf{I}]$  with identity matrix  $\mathbf{I}$  in  $\mathbb{R}^d$  and discrete points  $\mathbf{x}^e$ , a point  $\mathbf{x} \in \mathcal{B}_k$  is interpolated within each element as

$$\mathbf{x} \approx \mathbf{x}^h = \mathbf{N}\mathbf{x}^e. \quad (2.4)$$

The same holds for the reference configuration  $\mathbf{X} \approx \mathbf{X}^h$ , the displacement field  $\mathbf{u} \approx \mathbf{u}^h$  and the virtual displacement field  $\delta\varphi \approx \mathbf{v}^h$ . In here we drop the index  $k$  for convenience. In standard finite elements the discrete points  $\mathbf{x}$  are known as nodes while in IGA they are called control points. For standard FE basis functions, Lagrange polynomials are used. Different choices are possible but not considered in this work. The isogeometric basis of local splines will be discussed in Sec. 2.3. The discretized weak form is written as

$$\mathbf{v}^T [\mathbf{f}_{\text{int}} + \mathbf{f}_c] = \mathbf{0}, \quad \forall \mathbf{v} \in \mathcal{V}^h, \quad (2.5)$$

with the internal forces

$$\mathbf{f}_{\text{int}} = \begin{cases} \int_{\mathcal{S}} \mathbf{N}_{,\alpha}^{\text{T}} \sigma^{\alpha\beta} \mathbf{N}_{,\beta} da, & \text{for } \mathcal{S}, \\ \int_{\mathcal{B}} \mathbf{N}_{,x} \boldsymbol{\sigma} dv, & \text{for } \mathcal{B}, \end{cases} \quad (2.6)$$

and the contact forces

$$\mathbf{f}_{\text{c}} = \int_{\Gamma_{\text{c}}} \mathbf{N}^{\text{T}} \mathbf{t}_{\text{c}} da. \quad (2.7)$$

An overview of computational contact mechanics is given briefly in the next section.

## 2.2 Computational contact formulation

In this section, a brief summary of the theory of computational contact mechanics is given. For more detailed information, the work by [Wriggers \(2006\)](#) is recommended. Here, the penalty method is used in order to model contact. The gap vector  $\mathbf{g}$  between two points  $\mathbf{x}_{\text{I}}$  and  $\mathbf{x}_{\text{II}}$  on the surfaces  $\Gamma_{\text{I}}$  and  $\Gamma_{\text{II}}$  is given by

$$\mathbf{g} = \mathbf{x}_{\text{I}} - \mathbf{x}_{\text{II}}. \quad (2.8)$$

The closest projection point  $\mathbf{x}_p = \mathbf{x}_{\text{II}}$  is obtained by orthogonal projection of  $\mathbf{x}_{\text{I}}$  onto  $\Gamma_{\text{II}}$  and represents the minimum distance. The contact traction is expressed as  $\mathbf{t}_{\text{c}} = \mathbf{t}_{\text{n}} + \mathbf{t}_{\text{t}}$  by its components in normal and tangential direction. To each point in contact a traction in normal direction

$$\mathbf{t}_{\text{n}}(\mathbf{x}_k) = \begin{cases} -\varepsilon_{\text{n}} g_{\text{n}} \mathbf{n}_p, & g_{\text{n}} < 0 \\ 0, & g_{\text{n}} \geq 0 \end{cases} \quad (2.9)$$

is applied. The traction is proportional to the normal gap  $g_{\text{n}} = (\mathbf{x}_{\text{I}} - \mathbf{x}_p) \cdot \mathbf{n}_p$ , the surface outward normal  $\mathbf{n}_p$  at  $\mathbf{x}_p$  and the constant penalty parameter  $\varepsilon_{\text{n}}$ . The tangential contact traction  $\mathbf{t}_{\text{t}}$  during frictional sliding is given by Coulomb's law as

$$\mathbf{t}_{\text{t}} = -\mu p \frac{\dot{\mathbf{g}}_{\text{t}}}{\|\dot{\mathbf{g}}_{\text{t}}\|}. \quad (2.10)$$

Here, we find the friction coefficient  $\mu$ , the contact pressure  $p = \|\mathbf{t}_{\text{n}}\|$  and the relative tangential sliding velocity  $\dot{\mathbf{g}}_{\text{t}}$ . The tangential contact slip  $\mathbf{g}_{\text{t}}$  consists of the reversible  $\Delta \mathbf{g}_{\text{e}}$  and irreversible  $\mathbf{g}_{\text{s}}$  part

$$\mathbf{g}_{\text{t}} = \Delta \mathbf{g}_{\text{e}} + \mathbf{g}_{\text{s}}. \quad (2.11)$$

Whether sticking or slipping is present, the slip criterion

$$f_{\text{s}} = \|\mathbf{t}_{\text{t}}\| - \mu p \quad (2.12)$$

is used. It holds sliding if  $f_{\text{s}} = 0$  and sticking for  $f_{\text{s}} < 0$ . The examples presented in this work deal with frictionless and frictional contact. For frictionless contact, the tangential traction  $\mathbf{t}_{\text{t}}$  vanishes and the contact traction is given by  $\mathbf{t}_{\text{c}} = \mathbf{t}_{\text{n}}$ . The computation of the contact integrals is performed using the two-half pass algorithm by [Sauer and De Lorenzis \(2013\)](#). This algorithm evaluates the contact traction on each body separately. Further information concerning the implementation and formulation of the frictional contact computation the work of [Sauer and De Lorenzis \(2015\)](#) is recommended.

## 2.3 LR B-spline fundamentals

Locally Refined B-splines (LR B-splines) were first introduced by [Dokken et al. \(2013\)](#) and further worked on by [Bressan \(2013\)](#) and [Johannessen et al. \(2014\)](#). The core idea of LR B-splines is to

break the tensor-product mesh structure of classical B-splines to obtain a local representation of the parameter space. As introduced in the B-spline theory, a knot vector  $\Xi$  of size  $n + p + 1$  generates  $n$  linearly independent basis functions of order<sup>2</sup>  $p$ . The local representation of the parameter space and the geometric discretization is obtained by splitting the global knot vector  $\Xi = [\xi_1, \dots, \xi_{n+p+1}]$  into local knot vectors  $\Xi_i = [\xi_i, \dots, \xi_{i+p+1}]$  each constructing a single basis function. The basis functions are defined by the Cox-de Boor recursion formula which depends on the local knot vector  $\Xi_i$  and desired polynomial order  $p$ , see [Cox \(1971\)](#) and [De Boor \(1972\)](#). For  $p = 0$

$$N_i^0(\xi_i, \xi_{i+1}) = \begin{cases} 1, & \text{if } \xi_i \leq \xi < \xi_{i+1}, \\ 0, & \text{otherwise,} \end{cases} \quad (2.13)$$

and for  $p > 0$

$$N_i^p(\xi) = \frac{\xi - \xi_i}{\xi_{i+p} - \xi_i} N_i^{p-1}(\xi_i, \dots, \xi_{p+i}) \frac{\xi_{i+p+1} - \xi}{\xi_{i+p+1} - \xi_{i+1}} N_{i+1}^{p-1}(\xi_{i+1}, \dots, \xi_{p+i+1}). \quad (2.14)$$

The local representation of the B-spline basis  $B_{i,j}^{p,q}(\xi, \eta)$  in two dimensions of order  $p$  and  $q$  is defined as a separable function  $B : \mathbb{R}^2 \rightarrow \mathbb{R}$

$$B_{i,j}^{p,q}(\xi, \eta) = N_i^p(\xi) M_j^q(\eta). \quad (2.15)$$

The properties of the LR B-splines follow directly from standard isogeometric analysis. The basis is non-negative, forms a partition of unity and the resulting geometry lies within its convex hull. The continuity across the element boundaries  $C^{p-m}$  is defined by the polynomial order  $p$  and the multiplicity of the knot vector entry  $m$ . An LR B-spline surface  $\mathcal{S}(\xi, \eta)$  is then constructed by a set of control points  $\mathbf{x}_{i,j}$  and the local basis functions

$$\mathcal{S}(\xi, \eta) = \sum_{i=1}^n \sum_{j=1}^m B_{i,j}^{p,q}(\xi, \eta) \mathbf{x}_{i,j}, \quad (2.16)$$

with  $n, m$  as the number of single basis functions in each parametric dimension. To ensure that LR B-splines keep the partition of unity property during local refinement the basis functions are multiplied by a scaling weight  $\gamma \in (0, 1]$

$$\mathcal{S}(\xi, \eta) = \sum_{i=1}^n \sum_{j=1}^m B_{i,j}^{p,q}(\xi, \eta) \mathbf{x}_{i,j} \gamma_{i,j}. \quad (2.17)$$

### 2.3.1 Locally refined meshes

The local representation of B-splines leads to new possibilities how the mesh of the parameter space can be constructed. The ability of local refinement of these so called LR meshes is the major advantage in comparison to classical tensor meshes. In [Fig. 2.1](#) a series of LR meshes in the bivariate case are illustrated. The basis is a quadratic tensor mesh spanned by open knot vectors in  $\xi$  and  $\eta$  direction.

---

<sup>2</sup>It is also known as degree

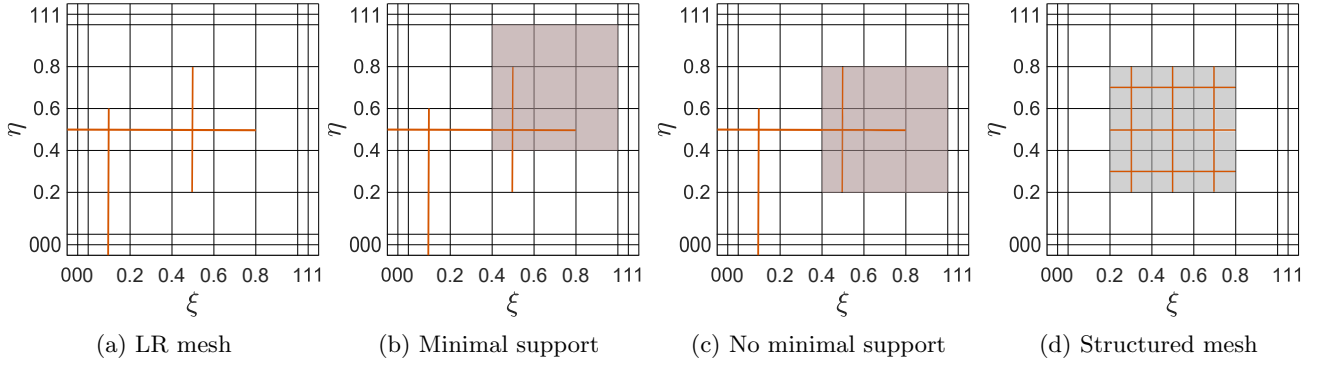


Figure 2.1: LR meshes constructed by meshline insertion (marked in orange) into a tensor mesh of a bivariate parameter space. (a) Example of an LR mesh. (b) LR B-spline basis that has minimal support. (c) LR B-spline basis that does *not* have minimal support. (d) Local refinement of an LR B-spline by a *structured mesh*.

The LR mesh is the result of a series of line insertions into the initial tensor mesh. These lines never stop in the center of an element (knot span) and each line is inserted one after another. As a knot vector of an LR B-spline basis function has size of  $p + 2$  knot value entries, the meshlines cross at least  $p + 2$  knots. A meshline extension can be either a new meshline, an elongation of an existing one, a joining of two meshlines or the increase of the multiplicity of a meshline. In the bi-variate case, horizontal and vertical meshlines can be inserted. The point of increasing multiplicity would decrease the continuity of the LR B-spline. Any type of meshline insertion causes that a local basis loses the property of minimal support. An LR B-spline has minimal support if its interior space is not traversed by any other meshline. As the basis of the LR B-spline (marked in gray) in Figure 2.1b is not traversed by any meshline completely it has minimal support. The LR B-spline basis marked in the Fig. 2.1c does not have minimal support. Its interior space is traversed by the vertical meshline  $\ell_v = 0.5 \times [0.2, 0.8]$ . Fig. 2.1d illustrates a specific fashion of meshline insertions. The refinement by structured meshes splits the entire support of an LR B-spline basis by horizontal and vertical meshlines equally. If an LR B-spline loses the property of minimal support the refinement is performed that is discussed in the next section.

### 2.3.2 Local refinement

In general, the refinement of LR B-splines is realized by single knot insertion. From the classical theory it is known that this enriches the basis while the geometry remains unchanged. The insertion of a single knot  $\hat{\xi}$  into the knot span  $\xi_i = [\xi_{i-1}, \xi_i]$  of a local knot vector  $\Xi$  of size  $p + 2$  yields to a knot vector of size  $p + 3$ . Consequently, two locally refined B-splines are generated by splitting  $\Xi$  of the enlarged LR B-spline. The resulting local knot vectors  $\Xi_1$  and  $\Xi_2$  of size  $p + 2$  are

$$\begin{aligned} \Xi &= [\xi_1, \dots, \xi_{i-1}, \xi_i, \dots, \xi_{p+2}] \\ \Xi_1 &= [\xi_1, \dots, \xi_{i-1}, \hat{\xi}, \xi_i, \dots, \xi_{p+1}] \\ \Xi_2 &= [\xi_2, \dots, \xi_{i-1}, \hat{\xi}, \xi_i, \dots, \xi_{p+2}] \end{aligned} \quad (2.18)$$

The following relation for an LR B-spline basis in one parametric direction on the LR mesh is then given by

$$\gamma N_{\Xi}^p(\xi) = \gamma_1 N_{\Xi_1}^p(\xi) + \gamma_2 N_{\Xi_2}^p(\xi). \quad (2.19)$$

with

$$\begin{aligned} \gamma_1 &= \alpha_1 \gamma, \\ \gamma_2 &= \alpha_2 \gamma. \end{aligned} \quad (2.20)$$

The associated  $\alpha_{1,2}$  are determined by

$$\alpha_1 = \begin{cases} 1, & \xi_{p+1} \leq \hat{\xi} < \xi_{p+2}, \\ \frac{\hat{\xi} - \xi_1}{\xi_{p+1} - \xi_1}, & \xi_1 < \hat{\xi} < \xi_{p+1}, \end{cases} \quad (2.21)$$

$$\alpha_2 = \begin{cases} \frac{\xi_{p+2} - \hat{\xi}}{\xi_{p+2} - \xi_2}, & \xi_2 < \hat{\xi} < \xi_{p+2}, \\ 1, & \xi_1 < \hat{\xi} \leq \xi_2. \end{cases}$$

Considering the knot  $\hat{\xi} = 0.375$  is inserted into the knot vector  $\Xi = [0, 0.25, 0.5, 0.75]$  constructing the quadratic basis function  $N_{\Xi}^2$ . As illustrated in Fig. 2.2, the former basis function is separated into two new functions each describing the LR B-spline basis functions  $\gamma\alpha_1 N_{\Xi_1}^2$  and  $\gamma\alpha_2 N_{\Xi_2}^2$ .

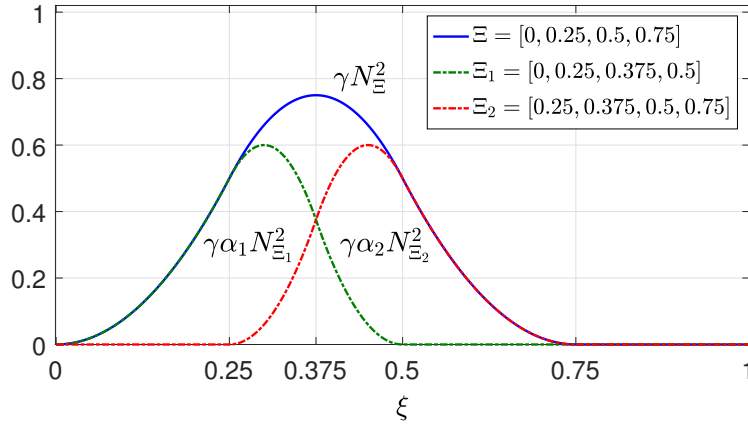


Figure 2.2: The original basis function of the knot vector  $\Xi$  is split by knot insertion at  $\xi = 0.375$  into two local basis functions characterized by the knot vectors  $\Xi_1$  and  $\Xi_2$

The refinement process for bivariate functions is performed in one parametric direction at a time, i.e. first all horizontal meshlines are inserted and then all verticals (or vice versa). Consider, two local knot vectors  $\Xi$  and  $\mathcal{H}$ , one in each parametric direction. For a weighted, bivariate LR B-spline basis  $\gamma B_{\Xi}^{p,q}(\xi, \eta)$  with  $\Xi = [\Xi, \mathcal{H}]$  the following relation is given

$$\begin{aligned} \gamma B_{\Xi}^{p,q}(\xi, \eta) &= \gamma N_{\Xi}^p(\xi) M_{\mathcal{H}}^q(\eta), \\ &= \gamma (\alpha_1 N_{\Xi_1}^p(\xi) + \alpha_2 N_{\Xi_2}^p(\xi)) M_{\mathcal{H}}^q(\eta), \\ &= \gamma_1 B_{\Xi_1}^{p,q}(\xi, \eta) + \gamma_2 B_{\Xi_2}^{p,q}(\xi, \eta), \end{aligned} \quad (2.22)$$

for the case if  $\Xi$  is split into  $\Xi_{1,2}$ . The refinement process is depicted by two main steps. At first all LR B-spline basis functions whose support is traversed by meshline extensions will be split. The second step is to check every newly created basis function if it has minimal support. In the case that a newly created LR B-spline does not have minimal support an additional splitting is performed. By splitting  $\gamma B_{\Xi}^{p,q}(\xi, \eta)$  two different cases can occur by creating the new LR B-spline basis functions  $\gamma_j B_{\Xi_j}^{p,q}(\xi, \eta)$ , with  $j = 1, 2$ . First, the LR B-spline does not exist and a new LR B-spline is created. In this case the new control point  $\mathbf{x}_j$  is a copy to the control point  $\mathbf{x}$  of the parent LR B-spline  $\mathbf{x}_j = \mathbf{x}$ . The weight  $\gamma_j$  is set by Eq. (2.20). Secondly, if  $B_{\Xi_j}^{p,q}(\xi, \eta)$  already exists the control point and the weight are set to

$$\mathbf{x}_j = \frac{\mathbf{x}_j \gamma_j + \mathbf{x} \gamma \alpha_j}{\gamma_j + \alpha_j \gamma}, \quad (2.23)$$

and

$$\gamma_j = \gamma_j + \gamma\alpha_j. \quad (2.24)$$

After the splitting the former LR B-spline  $\gamma B_{\Xi}^{p,q}(\xi, \eta)$  is deleted in both cases. The algorithm proceeds with the second step and checks if the support of the new local basis functions is traversed by any existing meshline. If one does not have minimal support the first step is performed again. Note that at every point of the refinement process the partition of unity will be kept and the geometric mapping will be left unchanged. It is important to ensure that the resulting spline space is linearly independent. In the bivariate case this can be guaranteed by only using primitive meshline extensions<sup>3</sup>, see [Mourrain \(2014\)](#). In this work, all meshline extensions are formulated as primitives.

### 3 Geometric modeling using LR NURBS

So far non-rational LR B-splines have been discussed. In this section, their extension to Locally Refined Non-Uniform *Rational* B-Splines (LR NURBS) is introduced. With an LR NURBS representation of objects one gains the ability to describe many geometries which cannot be represented by polynomials exactly. Especially conic sections, ellipsoids, spheres, cylinders, etc. can be constructed by a projective transformation of piecewise quadratic curves exactly, see [Farin \(1992\)](#). This is one of the defining features of isogeometric analysis.

#### 3.1 LR NURBS

The fundamentals of standard NURBS in isogeometric analysis can be found in, e.g. [Hughes et al. \(2005\)](#). Combining NURBS with the LR B-spline theory from Sec. 2.3 their extension to LR NURBS follows. An LR NURBS object in  $\mathbb{R}^d$  is constructed by the projective transformation of an LR B-spline entity in  $\mathbb{R}^{d+1}$ . The control points of the LR NURBS object result from the projective transformation

$$(\mathbf{x}_i)_k = \frac{(\mathbf{x}_i^w)_k}{w_i}, \quad k = 1, \dots, d, \quad \text{where } w_i = (\mathbf{x}_i^w)_{d+1}, \quad (3.1)$$

with  $(\mathbf{x}_i)_k$  as the  $k^{\text{th}}$  component of the vector  $\mathbf{x}_i$  and  $w_i$  as the  $i^{\text{th}}$  weight. The first  $d$  entries represent the spatial coordinates and the  $d+1$ 's entry the weight e.g.  $\mathbf{x}_i^w = [x_i, y_i, z_i, w_i]$  for  $d = 3$ . To generalize this relation the weighting function for the bivariate case is introduced by

$$W(\xi, \eta) = \sum_{i=0}^n \sum_{j=0}^m B_{i,j}^{p,q}(\xi, \eta) w_{i,j}. \quad (3.2)$$

$B_{i,j}^{p,q}(\xi, \eta)$  are the standard LR B-spline basis functions and the transformation is applied by dividing every point of the curve by  $W(\xi, \eta)$ . Each element of  $\mathcal{S}(\xi, \eta)$  is a polynomial which is divided by another polynomial of the same order. The resulting LR NURBS basis is then defined as

$$R_{i,j}^{p,q}(\xi, \eta) = \frac{B_{i,j}^{p,q}(\xi, \eta) w_{i,j}}{W(\xi, \eta)} = \frac{B_{i,j}^{p,q}(\xi, \eta) w_{i,j}}{\sum_{\hat{i}=0}^n \sum_{\hat{j}=0}^m B_{\hat{i},\hat{j}}^{p,q}(\xi, \eta) w_{\hat{i},\hat{j}}}. \quad (3.3)$$

With a set of control points  $\mathbf{x}_{i,j}$  and the scaling weights  $\gamma_{i,j}$  the LR NURBS surface is defined as

$$\mathcal{S}(\xi, \eta) = \sum_{i=0}^n \sum_{j=0}^m R_{i,j}^{p,q}(\xi, \eta) \mathbf{x}_{i,j} \gamma_{i,j}. \quad (3.4)$$

---

<sup>3</sup>(a) meshline spanning  $p + 1$  elements, (b) elongating a meshline by one element, (c) raising the multiplicity of a meshline (length  $p + 1$  elements)



The properties of the LR NURBS basis, such as the continuity and their support, follow directly from the knot vectors as before. The basis is still non-negative and it forms a partition of unity. This leads to the strong convex hull property of the NURBS. Note that the weights are separated from any explicit geometric representation. The weights are each associated to a specific control point and a manipulation of them leads to a change of the resulting geometry. In the case that all weights are equal the surface is again a polynomial and  $R_{i,j}^{p,q}(\xi, \eta) = B_{i,j}^{p,q}(\xi, \eta)$  results. Therefore, LR B-splines are a special case of LR NURBS. In order to locally refine an LR NURBS object it is necessary to take special care of the weights. Before the refinement procedure starts, the projective control points  $\mathbf{x}_{i,j}^w$  of the LR NURBS are computed by Eq. (3.1). The weights  $w_{i,j}$  are added to  $\mathbf{x}_{i,j}^w$  and treated as the fourth part of the control points. This results in

$$\mathbf{x}_{i,j}^w = [x_{i,j}w_{i,j}, y_{i,j}w_{i,j}, z_{i,j}w_{i,j}, w_{i,j}]. \quad (3.5)$$

After the refinement process the control points are transformed back by dividing the spatial coordinates by their associated weight. Note that while the refinement is performed,  $w_{i,j}$  is treated in the same way as the control points.

### 3.2 Bézier extraction operator for LR NURBS

This section discusses the Bézier extraction of LR NURBS which is an advantageous technique for the decomposition of splines into their Bézier elements. The Bézier extraction operator allows the embedding of isogeometric analysis into a standard finite element framework in a suitable way. The Bézier extraction of NURBS is introduced by [Borden et al. \(2011\)](#) and of T-splines by [Scott et al. \(2011\)](#). The basis function in one parametric direction of an LR NURBS element  $\Gamma^e$  within the knot span  $\tilde{\xi}$  is expressed in terms of a set of Bernstein polynomials  $\mathbf{B}(\tilde{\xi})$  and a linear operator  $\mathbf{c}_a^e$ . Each local basis function  $N_a^e(\tilde{\xi})$  of an element  $\Gamma_{\square}^e$  can be expressed by

$$N_a^e(\tilde{\xi}) = \mathbf{c}_a^e \mathbf{B}(\tilde{\xi}). \quad (3.6)$$

Here,  $a = 1, 2, \dots, n^e$  and  $n^e$  is the number of nonzero basis functions on  $\Gamma_{\square}^e$ . In general, the coefficients of  $\mathbf{c}_a^e$  are calculated by a knot insertion algorithm that can be found in [Scott et al. \(2011\)](#). This is not sufficient for the unstructured LR meshes of LR NURBS and an additional mapping has to be included. Consider the element  $\Gamma_{\square}^e$  with  $\tilde{\xi} = [0, 0.1]$  marked in yellow in Fig. 3.1 (left). The support of the local basis function  $N_a^e(\xi)$  marked in gray is spanned by the local knot vector  $\hat{\xi} = [0, 0.2, 0.4, 0.6]$  in  $\xi$ -direction. The basis function is non-zero within the domain of  $\Gamma_{\square}^e$ . From  $\hat{\xi}$  follows that  $\hat{\mathbf{c}}_a^e$  is defined within the domain  $\hat{\xi} = [0, 0.2]$  and exceeds  $\tilde{\xi} = [0, 0.1]$  (the domain of  $\Gamma_{\square}^e$ ), see Fig. 3.1 (right).

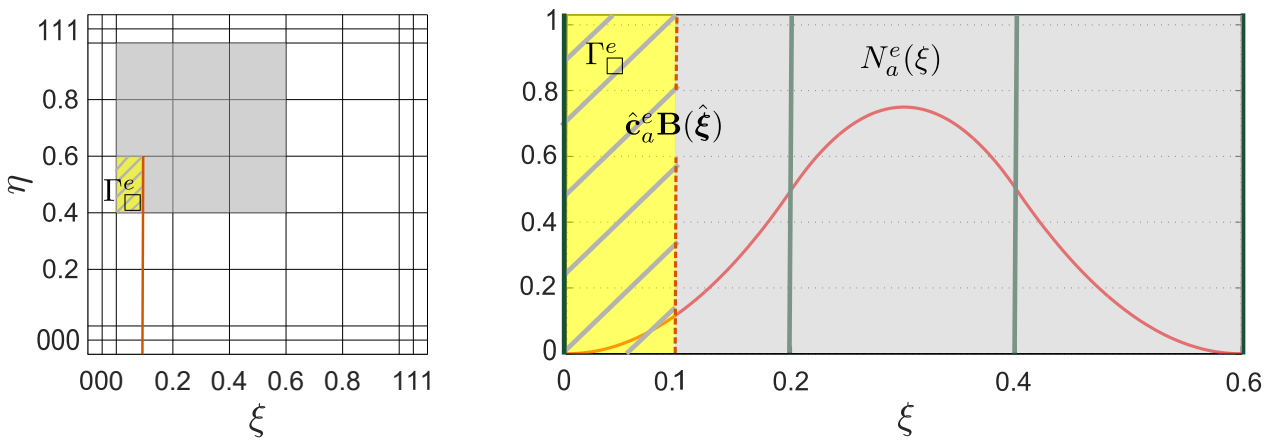


Figure 3.1: Bivariate LR mesh (left) and the local basis function of a quadratic LR NURBS in one parametric direction (right). The support of  $N_a^e(\xi)$  is represented by  $\hat{\mathbf{c}}_a^e \mathbf{B}(\hat{\xi})$  in the knot span  $\hat{\xi} = [0, 0.2]$  exceeding the actual domain of  $\Gamma_{\square}^e$ .

For this issue, a mapping of  $\hat{\mathbf{c}}_a^e$  to  $\mathbf{c}_a^e$  is performed using the transformation matrix  $\mathbf{T}_a^e$  such that

$$\mathbf{c}_a^e = \hat{\mathbf{c}}_a^e \mathbf{T}_a^e, \quad (3.7)$$

holds. The transformation matrix follows from

$$\mathbf{c}_a^e \mathbf{B}(\tilde{\boldsymbol{\xi}}) = \hat{\mathbf{c}}_a^e \mathbf{B}(\hat{\boldsymbol{\xi}}). \quad (3.8)$$

After some algebraic manipulations this equation is expressed as

$$(\mathbf{c}_a^e)^{\mathbf{T}} = \left( \mathbf{B}(\tilde{\boldsymbol{\xi}}) \right)^{-1} \mathbf{B}(\hat{\boldsymbol{\xi}}) (\hat{\mathbf{c}}_a^e)^{\mathbf{T}}. \quad (3.9)$$

With

$$\mathbf{T}_a^e = \left( \mathbf{B}(\tilde{\boldsymbol{\xi}}) \right)^{-1} \mathbf{B}(\hat{\boldsymbol{\xi}}), \quad (3.10)$$

the mapping of the Bernstein polynomials from  $\mathbf{B}(\hat{\boldsymbol{\xi}})$  to  $\mathbf{B}(\tilde{\boldsymbol{\xi}})$  is performed. In case that  $\tilde{\boldsymbol{\xi}} = \hat{\boldsymbol{\xi}}$ ,

$$\mathbf{B}(\tilde{\boldsymbol{\xi}}) = \mathbf{B}(\hat{\boldsymbol{\xi}}), \quad (3.11)$$

$$\left( \mathbf{B}(\tilde{\boldsymbol{\xi}}) \right)^{-1} \mathbf{B}(\hat{\boldsymbol{\xi}}) = \mathbf{I}, \quad (3.12)$$

and  $\mathbf{c}_a^e = \hat{\mathbf{c}}_a^e$  follows. With this formulation the basis functions having support in each element  $\Gamma_{\square}^e$  are expressed by Bernstein polynomials and the coefficients  $\mathbf{c}_a^e$ .

## 4 Adaptive local refinement and coarsening

In this section, a technique for adaptive local refinement and coarsening using LR NURBS discretizations is presented. The technique is formulated in the context of contact computations which is challenging. The reason is that frictional contact is history dependent and the contact properties need to be preserved while changing the discretization.

### 4.1 Adaptive local refinement

The adaptive local refinement technique necessitates an indicator for refinement. Commonly used indicators base on *A priori* error estimates using *A posteriori* error estimation providing reliable element error distribution, see e.g. [Ainsworth and Oden \(1997\)](#), [Johannessen et al. \(2014\)](#) and [Kumar et al. \(2015\)](#). In this work, error measures are not considered. The provided contact algorithm gives information of the location of the domain of major interest, the local contact domain. A refinement indicator is used to store for each contact element whether it is in contact or not. After the contact domain is determined the local refinement is performed by meshline extensions in the parameter space. All elements are refined by structured meshes that split all elements within the entire support of the basis functions, see Sec. 2.3. The refinement is performed until a prescribed *depth* (i.e. smallest element size) is obtained. In terms of sliding contact it is desirable to enlarge the domain for refinement to reduce the number of refinement steps. This further motivates to coarsen refined elements if contact is not anymore present. To automatically control the procedure of adaptive local refinement and coarsening, three parameters are set:

- $d_{\text{ref}}$  enlarges the refinement domain by a specified distance in both parametric directions. This reduces the number of refinement steps in the context of sliding contact.

- $d_{\text{safe}}$  specifies a safety domain at the refined boundary. Refinement is performed if contact is detected within this domain.  $d_{\text{safe}}$  ensures that the contact domain is at every time step locally refined.
- $d_{\text{crs}}$  specifies a maximum distance from the boundary of the contact domain to refined elements. Coarsening is performed if refined elements are present outside of this distance.

In Fig. 4.1 the parameters and a discretized surface using quadratic LR NURBS elements is sketched. In this example the refinement by structured meshes is applied to refine the entire support of all flagged elements. Due to the location of the contact domain and the parameter  $d_{\text{ref}}$  the refinement is performed by the orange marked meshline extensions. If the contact domain changes and refined elements are detected afar from the contact domain a coarsening step is performed.

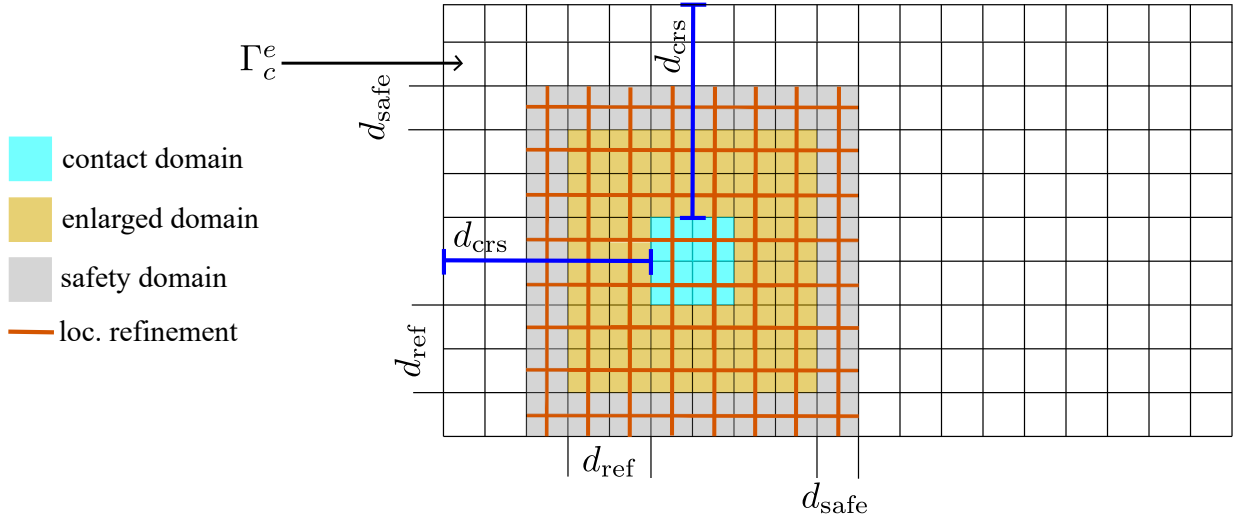


Figure 4.1: Sketch of a discretized surface using quadratic LR NURBS elements and the parameters  $d_{\text{ref}}$ ,  $d_{\text{safe}}$  and  $d_{\text{crs}}$ . Local refinement is considered in the three shown domains.

This procedure ensures that the contact domain and the neighboring elements are always represented in the desired discretization. The coefficients  $d_{\text{ref}}$ ,  $d_{\text{safe}}$  and  $d_{\text{crs}}$  can be set arbitrarily and a good choice is depending on the specific problem setup. A good compromise of the size of the locally refined domain and the number of refinement/coarsening steps is desirable. The coarsening is discussed in the next section.

## 4.2 Adaptive coarsening

The feature of coarsen LR meshes in the context of contact computations is challenging. The reasons are the unstructured parametric representation of LR NURBS and that frictional contact is history dependent from a computational point of view. The contact properties necessitate to be preserved during the process of coarsening and refinement. A technique for NURBS and T-spline coarsening is presented in [Thomas et al. \(2015\)](#). This technique is not available for LR NURBS on unstructured meshes with varying depths of refinement. To overcome this issue, the coarsening is explicitly coupled with the local refinement. The technique consists of six main steps to perform a consistent adaptive coarsening within the context of contact computations. The technique is sketched in Fig. 4.2 and the steps are as follows:

1. If coarsening is detected: Store the contact properties for each contact element  $\Gamma_c^e$  and the control point's position  $\mathbf{x}_{i,j}$  of the entire model (Fig. 4.2 (a)).
2. Obtain the initial, coarse discretization by loading the parametric representation of the unrefined, reference configuration.
3. Interpolate the geometry to obtain the current, deformed configuration in its initial parametric representation (Fig. 4.2 (b)). A simple interpolation of the control points is performed. This can lead to a geometric approximation error that is addressed in step (5).
4. Perform local refinement to obtain the desired, locally refined model (Fig. 4.2 (c)).
5. Reduce the geometric approximation error by comparing the deformed model before the coarsening step and the current model. The domains that remain unchanged in their parametric representation are restored.
6. Preserve the contact properties by mapping them to the current configuration.

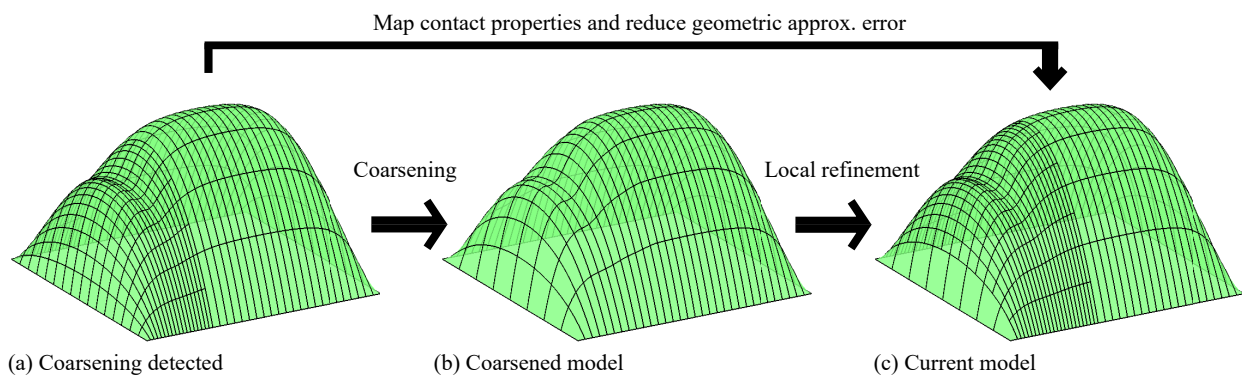


Figure 4.2: Sketch of the proposed coarsening and refinement procedure.

## 5 Numerical examples

The performance of the adaptive local refinement and coarsening technique using LR NURBS elements is illustrated in this chapter by several numerical examples. The first example is used for validation in which LR NURBS, standard NURBS and Lagrange elements are compared to an analytical solution. In the later examples, the performance of LR NURBS in the framework of frictionless and frictional contact is investigated. In the last example, the adaptive local refinement is applied to LR NURBS-enriched contact elements of a three-dimensional model with two deformable solids. To investigate the benefit of LR NURBS meshes comparisons to reference models with uniformly NURBS discretizations are made.

### 5.1 Inflation of a hemisphere

In the first example we consider the inflation of a solid membrane surface. The inflation of a spherical balloon can be described by an analytical formulation that is used for validation. The system is modeled as a hemisphere and the boundary conditions at  $Y = 0$  are chosen such that the symmetry of the model is maintained, see Fig. 5.1 (left). This model consists of five patches and the LR NURBS weights differ for each. The material is described by the incompressible Neo-Hookean material model

$$\sigma^{\alpha\beta} = \frac{\mu}{J} \left( A^{\alpha\beta} - \frac{a^{\alpha\beta}}{J^2} \right). \quad (5.1)$$

Here, we find the shear modulus  $\mu$ , the surface area change  $J$  and the contra-variant components of the metric tensor in the reference and current configuration  $A^{\alpha\beta}$  and  $a^{\alpha\beta}$ . The current radius of the hemisphere is denoted by  $r = \lambda R_0$  with initial radius  $R_0$  and pre-stretching  $\lambda = 1.1$ . The pre-stretching is applied to provide initial out-of-plane stiffness. The problem setup is similar to the one of [Sauer et al. \(2014\)](#) in which the balloon is modeled as 1/8th of a sphere with NURBS and Lagrange discretizations. Initially the model has the volume  $V_0 = 4\pi R_0^3/3$ . The volume is increased step-wise until it reaches  $V = 50 V_0$ . The analytical pressure-volume relation is given by

$$\frac{p_{\text{int}} R}{\mu} = 2 \left( \left( \frac{V_0}{V} \right)^{\frac{1}{3}} - \left( \frac{V_0}{V} \right)^{\frac{7}{3}} \right), \quad (5.2)$$

with the internal pressure  $p_{\text{int}}$ . It is used to investigate the behavior of different finite element discretizations.

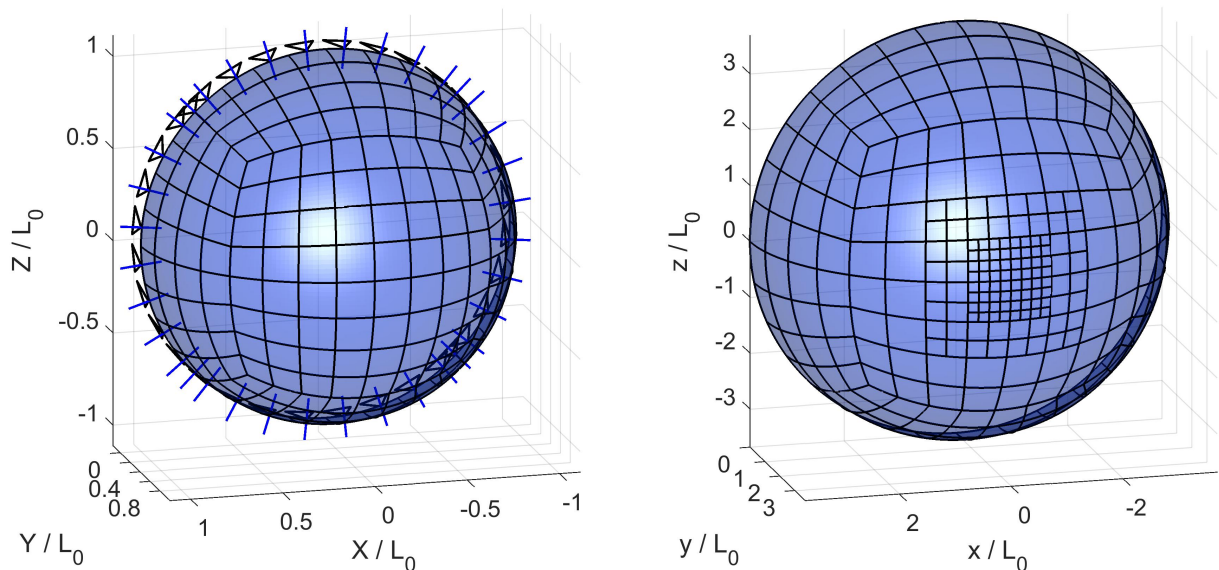


Figure 5.1: Inflation of a hemispherical membrane: Model setup in the initial configuration (left). Current configuration at  $V = 50 V_0$ , two times locally refined (right).

We now investigate the behavior of the proposed local refinement procedure using quadratic LR NURBS elements. Five different uniform meshes with quadratic LR NURBS discretizations are taken each as the starting point. The number of Gaussian quadrature points are the same for all elements, and  $n_{qp} = 3 \times 3$  is chosen. As an homogeneous hemisphere has no domain of major interest, the center is chosen manually to apply local refinement of depth two, see Fig. 5.1 (right). The performance of the five meshes is now compared to quadratic NURBS and quadratic Lagrange discretizations. The internal pressure error is shown in Fig. 5.2. The isogeometric elements behave as observed in [Sauer et al. \(2014\)](#) and show better convergence behavior than standard Lagrange elements. The LR NURBS meshes behave similar as the uniform NURBS meshes. Due to the homogeneous behavior of the hemisphere local refinement does not improve the numerical results significantly. But with this first example we can conclude that the applied local refinement procedure works successful and the computations with LR NURBS are valid. In the following examples the performance of adaptive local refinement with respect to the accuracy and the computational cost is investigated.

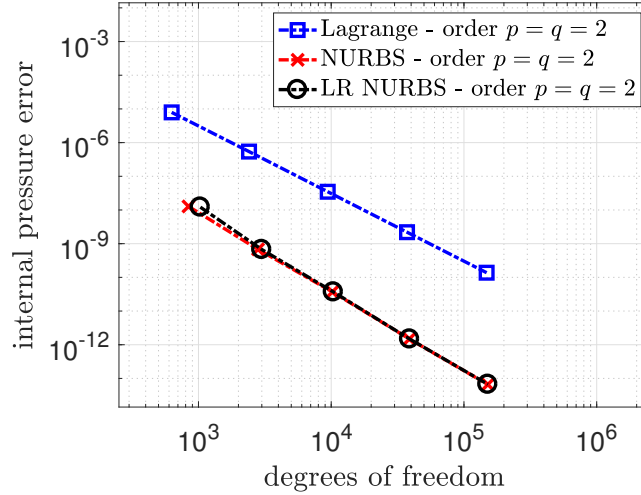


Figure 5.2: Inflation of a hemispherical membrane: Internal pressure error for meshes discretized by quadratic Lagrange, quadratic NURBS and quadratic LR NURBS elements in comparison to the analytical solution. There is no benefit in local refinement for a problem with a uniform solution.

## 5.2 Rigid sphere in contact with a square membrane sheet

The second example considers a square membrane surface with dimensions  $2L_0 \times 2L_0$  which is initially pre-stretched by  $\lambda = 1.1$ . The pre-stretching is applied to avoid the instability of the membrane formulation that does not support in-plane compression. A rigid sphere located at  $\mathbf{X} = [0, 0, L_0]$  with radius  $R_0 = L_0$  and is positioned gradually downwards until the bottom of the sphere reaches  $z = -L_0/2$  as shown in Fig. 5.3. The initial mesh consists of  $4 \times 4$  LR NURBS elements with each  $5 \times 5$  Gaussian quadrature points. The material behavior is the same as in the previous example. The boundaries at  $X = 2L_0$  and  $Y = 2L_0$  are fixed in all parametric directions. At  $X = 0$  and  $Y = 0$  the deformation is constraint to be zero in  $x$ - and  $y$ -direction, respectively. Contact between the rigid sphere and the membrane is treated by the penalty method with a penalty parameter

$$\varepsilon_n^{el} = \varepsilon_n^0 \cdot \left( \frac{l_{0x} l_{0y}}{l_{elx} l_{ely}} \right)^{p-1} \quad (5.3)$$

depending on the individual element size. Here, we find the polynomial order<sup>4</sup>  $p$  and the constant penalty parameter  $\varepsilon_n^0 = 10$  is chosen.

<sup>4</sup>The order in both parametric directions is set equally, i.e.  $q = p$

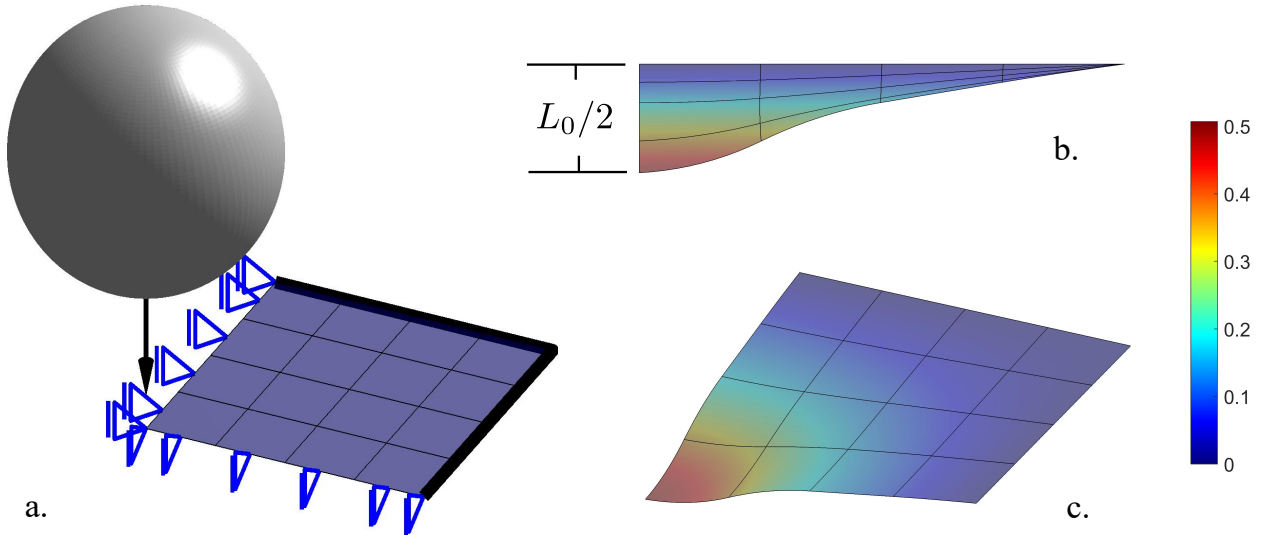


Figure 5.3: Rigid sphere in contact with a square membrane sheet: (a) Membrane surface model, boundary conditions and rigid sphere. (b), (c) Deformed membrane surface from two different points of view. The coloring shows the displacement of the membrane.

The contact domain is locally refined by the procedure described in Sec. 4. A series of resulting meshes for quadratic LR NURBS elements is illustrated in Fig. 5.4 from refinement depth one to five. A strong local aggregation of elements is obtained in the contact domain. In this first example the refinement domain is not enlarged by the coefficient  $d_{\text{ref}}$ .

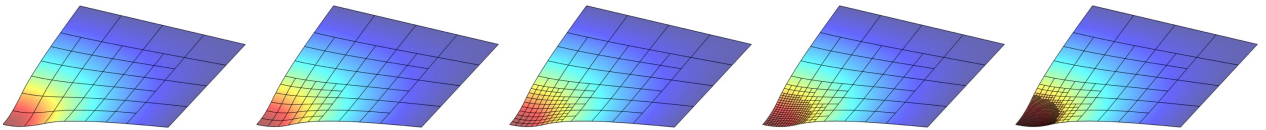


Figure 5.4: Rigid sphere in contact with a square membrane sheet: Deformation series with a locally refined contact domain. A refinement depth from one to five is applied. The coloring shows the displacement of the membrane.

The performance of LR NURBS meshes and uniform meshes using NURBS discretizations is investigated. The relative error

$$e_n^{\text{rel}} = \frac{|f_n^{\text{ref}} - f_n|}{|f_n^{\text{ref}}|} \quad (5.4)$$

of the normal contact force  $f_n$  is defined w.r.t. a reference solution. For the reference, a uniform mesh with cubic NURBS discretizations is taken. This model has more than  $5 \cdot 10^4$  dofs and  $\varepsilon_n^{\text{el}} > 10^6$  which is assumed to be accurate. The relative contact force error of LR NURBS and homogeneous meshes is illustrated in Fig. 5.5. The proposed local refinement technique using LR NURBS elements show a nice convergence behavior for quadratic and cubic elements. The most accurate results of the LR NURBS meshes for both orders are each achieved with a local contact domain consisting of elements with the same size as the reference model. It turns out that for cubic elements the obtained relative error decreases to  $\approx 8.7 \cdot 10^{-8}$  while for quadratic elements  $\approx 2.1 \cdot 10^{-4}$  is achieved. Since the penalty parameter is increased by Eq. (5.3) and it is depending on the polynomial order, the higher accuracy for cubic elements is expected. The dofs are reduced by a factor of more than 16 for LR NURBS meshes with quadratic and cubic elements at the fifth refinement depth. This is a huge decrease of the computational cost. In Tab. 5.1 the mesh properties and numerical results for cubic elements are listed. This example shows that with the local refinement procedure a high accuracy is achieved while decreasing the computational cost.

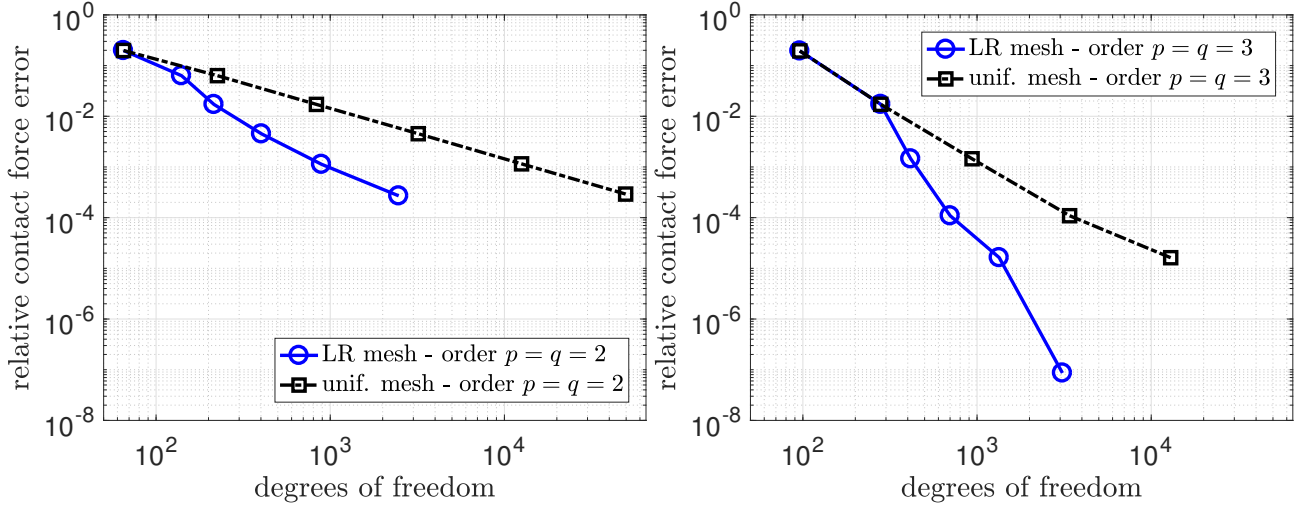


Figure 5.5: Rigid sphere in contact with a square membrane sheet: Relative error of the normal contact force for quadratic discretizations (left) and cubic discretizations (right). The error is defined w.r.t. a uniformly discretized mesh with cubic NURBS elements that is taken as the reference.

LR mesh	dofs	# el.	rel. error
depth 0	96	16	$1.95 \cdot 10^{-1}$
depth 1	280	64	$1.72 \cdot 10^{-2}$
depth 2	416	112	$1.45 \cdot 10^{-3}$
depth 3	701	211	$1.09 \cdot 10^{-4}$
depth 4	1340	430	$1.63 \cdot 10^{-5}$
depth 5	3092	1024	$8.63 \cdot 10^{-8}$

unif. mesh	dofs	# el.	rel. error
depth 0	96	16	$1.95 \cdot 10^{-1}$
depth 1	280	64	$1.72 \cdot 10^{-2}$
depth 2	936	256	$1.45 \cdot 10^{-3}$
depth 3	3400	1024	$1.09 \cdot 10^{-4}$
depth 4	12936	4096	$1.62 \cdot 10^{-5}$
reference mod.	50440	16384	—

Table 5.1: Rigid sphere in contact with a square membrane sheet: Comparison of the mesh parameters and the computational error between the LR mesh and the uniformly refined mesh. Cubic discretization is considered. Corresponding refinement depth have almost equal error but hugely different number of dofs.

In a second part of this example the performance of LR NURBS elements for different sizes of the contact domain is investigated. Computations for different radii of the rigid sphere are performed. The initial radius is set to  $R_0 = 1/10 L_0$  and is step-wise increased to  $R_0 = L_0$ . The different rigid spheres and the number of dofs resulting from local refinement of the contact domain are shown in Fig. 5.6.

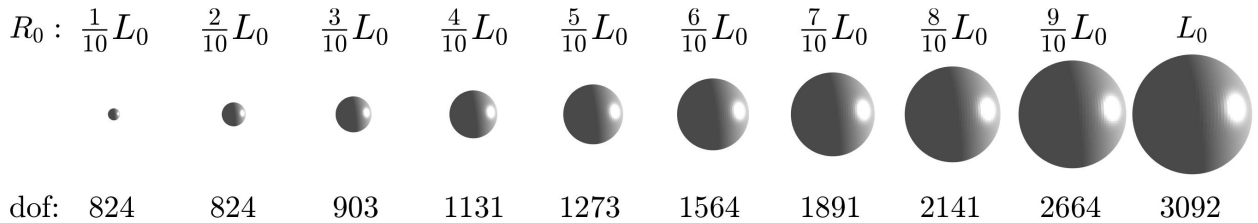


Figure 5.6: Rigid sphere in contact with a square membrane sheet: Different radii of the rigid sphere. Increasing the contact domain leads to an increase in the number of dofs of the LR NURBS meshes.

The sphere is positioned at  $X = Y = 0$  gradually to  $z = -R_0^i/2$ . The performance of LR NURBS meshes using cubic elements is investigated. Local refinement of depth five is applied. The relative error of the normal contact force is defined w.r.t. their uniformly discretized counterparts using cubic



NURBS elements. The smallest element size of each mesh is identical leading to the same value for  $\varepsilon_n^{el}$ . The relative contact force error with respect to the dofs for varying radii  $R_0^i$  is shown in Fig. 5.7.

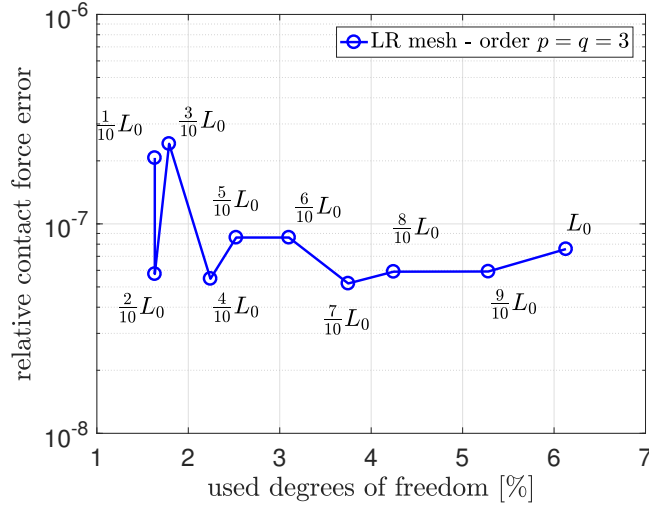


Figure 5.7: Rigid sphere in contact with a square membrane sheet: Relative error of the normal contact force. The error is defined w.r.t. a uniform mesh with cubic NURBS discretizations. The  $x$ -axis shows the ratio of the used dofs with respect to the reference model.

The LR NURBS meshes capture the results of the reference models nicely. A high accuracy is achieved while only using few dofs. The consequence for the entire computation is that for  $R_0^1 = 1/10L_0$  less than 2% of the time is used in comparison to the reference model. The time for the local refinement procedure is negligible small. This reduction of the computational effort while still achieving high accuracy demonstrates the benefit of the local refinement technique using LR NURBS.

### 5.3 Frictionless sliding contact

In the third example the performance of the adaptive local refinement and coarsening technique from Sec. 4 is investigated. For this issue, frictionless sliding contact is considered. The problem is setup as a rectangular solid membrane having dimensions  $8L_0 \times 2L_0$  with pre-stretching  $\lambda = 1.25$ . The boundaries are clamped. A rigid sphere with radius  $L_0$  is initially located at  $\mathbf{X} = \lambda \cdot [L_0, L_0, L_0]$  and first positioned downwards to  $\mathbf{x} = \lambda \cdot [L_0, L_0, L_0/2]$ . This is followed by a frictionless sliding along the entire surface until it reaches  $\mathbf{x} = \lambda \cdot [7L_0, L_0, L_0/2]$ , see Fig. 5.8 (left). The volume enclosed by the membrane is constraint to be constant so that it behaves like a cushion. The material and the computational parameter setup is the same as in the previous example. Due to the frictionless sliding the contact domain changes and the presented adaptive local refinement and coarsening procedure is applied to obtain highly resolved meshes in the contact domain. Fig. 5.8 (right) shows the deformed configuration after the downward displacement of the rigid sphere is applied. The locally refined domain is enlarged by setting an appropriate value for the parameter  $d_{\text{ref}}$ . In Fig. 5.9 two meshes resulting from the adaptive local refinement and coarsening technique are illustrated.

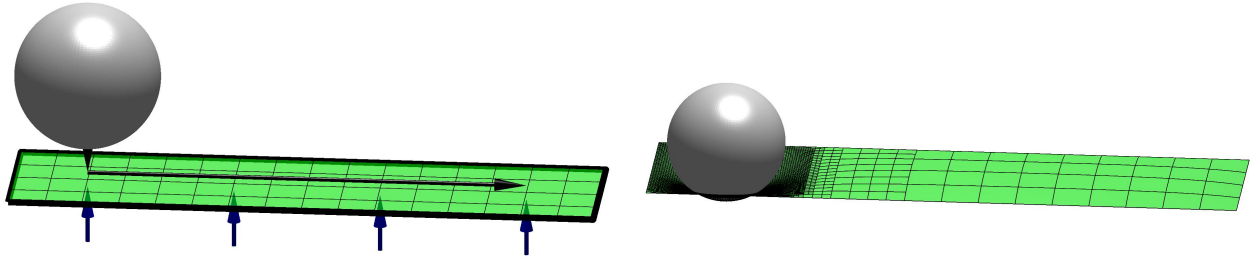


Figure 5.8: Frictionless sliding contact: Initial problem setup (left). The membrane is initially discretized by  $4 \times 16$  elements. The LR NURBS mesh, after the sphere is moved downward, is shown in the right figure. Local refinement of depth four is applied leading to a highly resolved mesh in the contact domain.

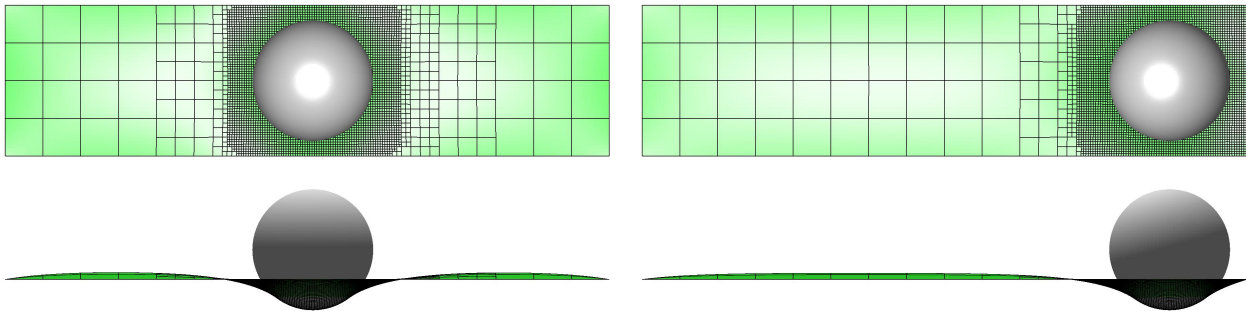


Figure 5.9: Frictionless sliding contact: Adaptive local refinement and coarsening of the model during frictionless sliding in top and side view. Highly resolved meshes within the local contact domain are obtained while the periphery is still represented with the coarse, initial setup.

It can be observed that during sliding only the contact domain has a high aggregation of LR NURBS elements. The performance of adaptive local refinement and coarsening using LR NURBS is investigated. For this issue, LR NURBS meshes are compared to uniformly discretized models using standard NURBS. The tangential and normal contact forces for the LR NURBS mesh and a uniformly discretized model are illustrated in Fig. 5.10. They match each other nicely for quadratic and cubic elements. The contact force  $f_t$  is small in comparison to  $f_n$  as the sliding is considered to be frictionless. Due to the problem setup  $f_t$  has peaks at those points where the sphere is located closest to the boundaries. The trend of  $f_n$  is constant except small deviations. These are caused by the volume constraint and the boundary conditions so that its maximum is reached where the sphere is located in the center of the model.

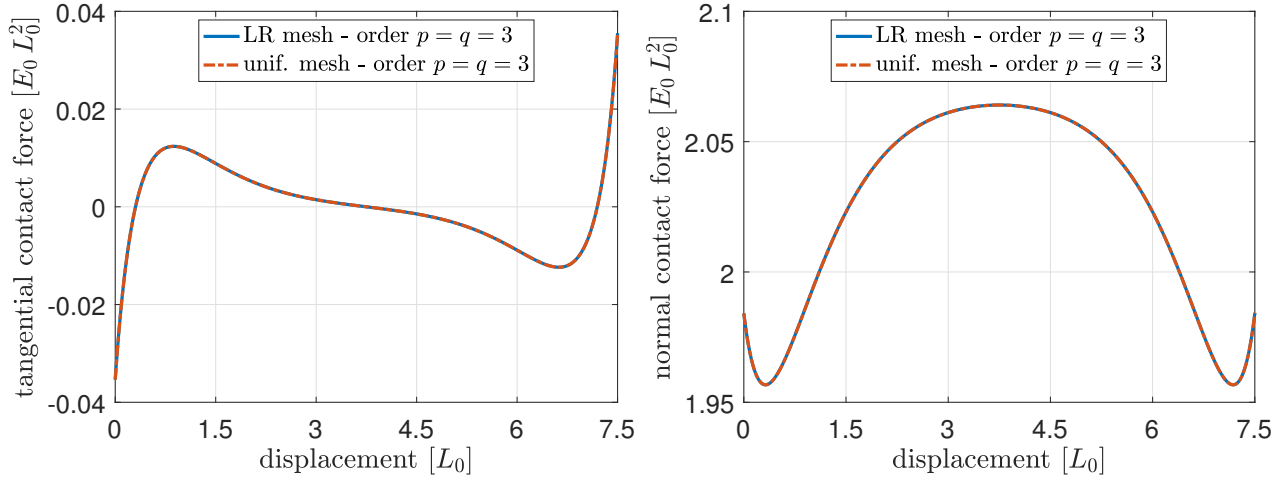


Figure 5.10: Frictionless sliding contact: Tangential (left) and normal (right) contact forces for both uniform and LR NURBS meshes. The LR NURBS mesh uses less than 30% of the dofs in comparison with the uniform mesh.

The performance of quadratic and cubic LR NURBS elements is investigated. The LR NURBS meshes are compared to their uniform counterparts using quadratic and cubic NURBS discretizations separately. In Fig. 5.11 the relative contact force error of  $f_t$  and  $f_n$  is illustrated. It can be observed that the LR NURBS meshes capture the reference solution nicely with less than 30% dofs in both examples. The reason for the high relative error of quadratic LR NURBS elements in comparison to cubic elements is the coarse periphery. The relative error results from the problem setup and the influence of the reaction forces on the entire system. Due to the higher interpolation of cubic LR NURBS elements the error coming from coarse elements is smaller. This phenomena is noticeable by investigating the relative error in normal direction. For both, quadratic and cubic elements the relative error in normal direction is slightly increased for rigid sphere positions in the center of the membrane. This increased error results from a coarse discretization of the left and right boundary of the model. The relative error in tangential direction is small in comparison to the error in normal direction. The evolution of the relative error in tangential direction shows abrupt changes. This results from the geometric approximation error of the coarsening steps. The influence of the geometric error can be neglected in this example as it is much smaller than the relative error of  $f_n$ . The parameters for the automatic control of the proposed technique are set appropriately leading to an almost constant evolution of the relative normal contact error. This example shows that the adaptive local refinement and coarsening technique using LR NURBS elements leads to highly accurate results while decreasing the computational cost.

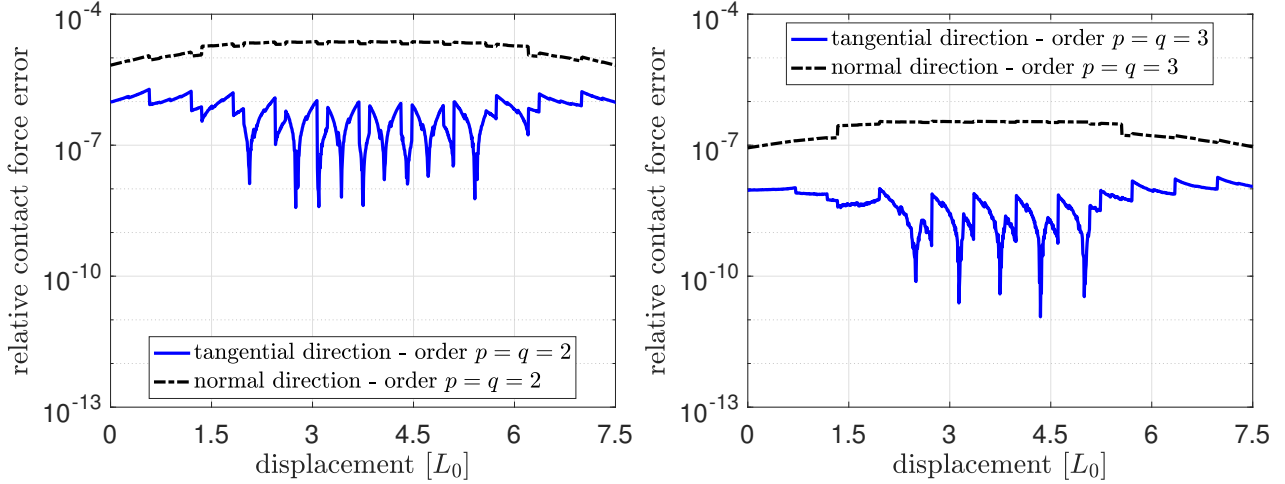


Figure 5.11: Frictionless sliding contact: Relative contact force error of LR NURBS. Quadratic LR NURBS elements are compared to quadratic, uniformly refined NURBS elements (left). Cubic LR NURBS elements are compared to cubic, uniformly refined NURBS elements (right). The LR NURBS mesh uses less than 30% of the dofs in comparison with the uniform mesh.

#### 5.4 Frictional contact of two deformable membranes

In the next example, the performance of LR NURBS in terms of frictional contact considering two deformable membranes is investigated. This example addresses two new aspects. First, the preservation of the contact properties during coarsening and refinement. Second, the local refinement and coarsening of two objects. We consider two deformable rectangular solid membranes with dimensions  $2L_0^u \times 0.5L_0^u$  and  $0.5L_0^l \times 2L_0^l$ . They are fixed at their boundaries in all parametric directions. A pre-stretching of  $\lambda = 1.5$  in their longitudinal direction is applied to avoid the compression-instability in terms of frictional contact. In Fig. 5.12 (left) the problem setup is shown. Both surfaces are inflated which is followed by a frictional sliding of the upper membrane along the entire domain of the lower one. The adaptive locally refined surfaces at the first contact detection are illustrated in Fig. 5.12 (right). The friction coefficient is set to  $\mu_{sf} = 0.25$  and the enclosed volume of both surfaces is constraint to be constant after inflation. The material behavior is the same as in the previous examples and  $5 \times 5$  Gaussian quadrature points are used. Contact is treated by the penalty method. The penalty parameter is increased by Eq. (5.3) with  $\varepsilon_0 = 80$  and is set equally in tangential and normal direction. The two-half-pass algorithm is used to evaluate the contact forces. Due to frictional sliding the contact domain changes and the presented adaptive local refinement and coarsening procedure is applied on both surfaces.

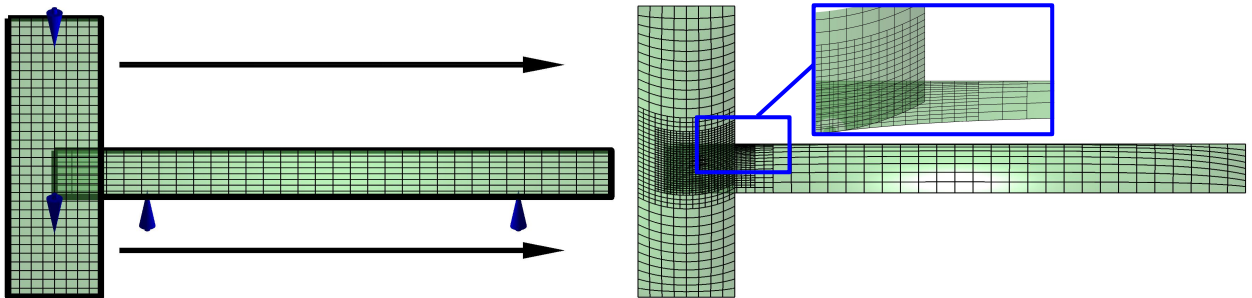


Figure 5.12: Frictional contact of two deformable membranes: Initial model setup (left). Initially, each membrane surface is discretized by  $8 \times 32$  elements. LR NURBS mesh at the time step of first contact detection (right). Local refinement of depth two is applied.

The performance of quadratic and cubic LR NURBS is investigated. The LR NURBS meshes are compared to their uniform counterparts using quadratic and cubic NURBS discretizations separately. The tangential contact force  $f_t$  and the normal contact force  $f_n$  acting on the lower surface are shown in Fig. 5.13. Their trend is as expected due to the problem setup and both models match each other nicely.

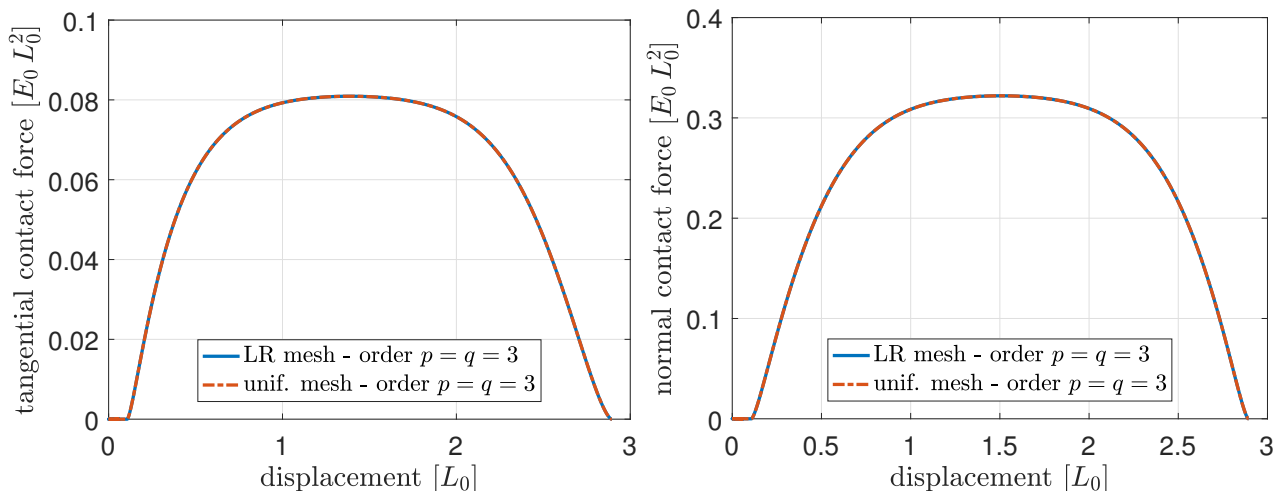


Figure 5.13: Frictional contact of two deformable membranes: Tangential (left) and normal (right) contact forces for both uniform and LR NURBS mesh. The LR NURBS mesh uses less than 30% of the dofs in comparison with the uniform mesh.

The contact forces tend to be zero at the beginning and end of the sliding process and small deviations are crucial for error investigations. For this issue, the relative contact force error with respect to the maximum normal contact force  $f_n^{\max}$  is investigated

$$e_t^{\text{rel}} = \frac{|f_t^{\text{ref}} - f_t|}{|f_n^{\max}|}, \quad \text{and} \quad e_n^{\text{rel}} = \frac{|f_n^{\text{ref}} - f_n|}{|f_n^{\max}|}. \quad (5.5)$$

In Fig. 5.14 the relative contact force error for quadratic and cubic LR NURBS is illustrated. The evolution of the relative error in normal direction shows a similar behavior as in the previous example. The cubic LR NURBS elements perform better than quadratic elements which is the result of the coarse periphery. The evolution of the relative error in tangential direction is more smooth than in the previous example. The reason is that the relative error of this frictional contact example is higher and the geometric approximation error shows no remarkable influence. A maximum relative error of  $\approx 3 \cdot 10^{-4}$  for quadratic LR NURBS discretizations is achieved. The relative error for cubic LR NURBS elements is much smaller and a maximum of  $\approx 3 \cdot 10^{-6}$  is achieved. With the setting of the coefficients for the automatic control less than 30% of the dofs of the reference models are used in both cases. This example shows that the technique of adaptive local refinement and coarsening is successfully applied to two deformable membrane surfaces in the framework of frictional contact. The computational cost is reduced while still achieving high accuracy. In the next example the adaptive local refinement and coarsening technique is applied to LR NURBS-enriched elements considering frictional contact.

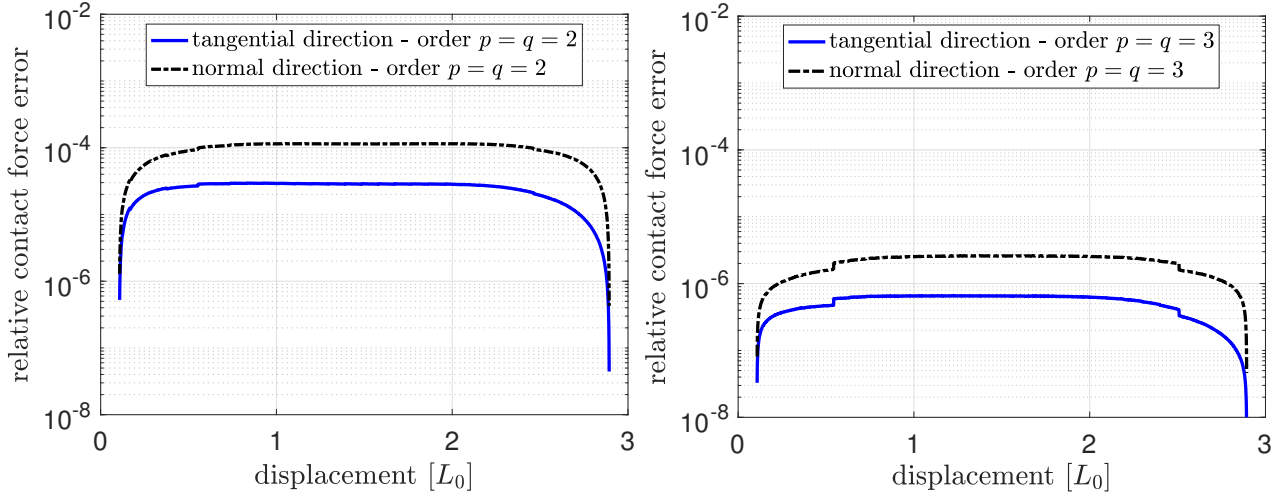


Figure 5.14: Frictional contact of two deformable membranes: Relative contact force error of LR NURBS. Quadratic LR NURBS elements are compared to quadratic, uniformly refined NURBS elements (left). Cubic LR NURBS elements are compared to cubic, uniformly refined NURBS elements (right). The LR NURBS mesh uses less than 30% of the dofs in comparison with the uniform mesh.

## 5.5 Frictional ironing contact between two deformable solids

Local refinement for general 3D isogeometrical models is challenging and the linear independency of LR meshes in 3D is not proven yet. To overcome this issue the NURBS-enrichment technique by [Corbett and Sauer \(2014\)](#) is extended to LR NURBS-enrichment.

### 5.5.1 LR NURBS-enriched finite elements

The core idea of this technique is to use standard finite Lagrange elements in the bulk domain and enriching the surface by isogeometric finite elements. The local refinement of LR NURBS-enriched elements is performed in two main steps

1. Local refinement of the LR NURBS surface
2. Pass the local refinement through all the Lagrange elements in thickness direction

The local refinement of the Lagrange elements involve the generation of irregular or hanging nodes. For the treatment of these irregular nodes the work by [Demkowicz et al. \(1989\)](#) is recommended.

### 5.5.2 Numerical results

In the last example we consider a deformable hollow hemisphere and a deformable block. Both three-dimensional solids have a quadratic LR NURBS-enriched contact surface. The hemisphere is discretized with three elements in its thickness direction and  $7 \times 7$  elements on the contact surface. The block is discretized with eight elements in its thickness direction and  $4 \times 40$  elements on the contact surface. For each contact element  $5 \times 5$  Gaussian quadrature points are used. The bulk domain is initially discretized by linear Lagrange finite elements. Initially, the block has dimensions  $1 L_0 \times 1 L_0 \times 10 L_0$  and the hollow hemisphere has the inner radius  $R_0^{\text{in}} = L_0/6$  and the outer radius  $R_0^{\text{out}} = L_0/2$ , see Fig. 5.15. The base of the block is fixed in all parametric directions. Periodic boundary

conditions are set to the left and right boundary of the block. First, a downward displacement of  $2/3R_0^{\text{out}}$  is applied to the top of the hollow hemisphere which is followed by a displacement of  $6L_0$  in tangential direction. The downward displacement is considered to be frictionless while the tangential displacement is considered to be frictional. The solids follow an isotropic, non-linear Neo-Hookean material model by [Zienkiewicz et al. \(2005\)](#)

$$\boldsymbol{\sigma} = \frac{\Lambda}{\det(\mathbf{F})} (\ln(\det(\mathbf{F}))) \mathbf{I} + \frac{\mu}{\det(\mathbf{F})} (\mathbf{F}\mathbf{F}^T - \mathbf{I}), \quad (5.6)$$

with the deformation gradient  $\mathbf{F}$  and the identity tensor  $\mathbf{I}$ . The Lamé constants  $\Lambda$  and  $\mu$  are expressed in terms of the Poisson's ratio  $\nu$  and Young's modulus  $E$  by

$$\mu = \frac{E}{2(1+\nu)} \quad \text{and} \quad \Lambda = \frac{2\mu\nu}{1-2\nu}. \quad (5.7)$$

With  $\nu_1 = \nu_2 = 0.3$  for both solids and  $E_1 = E_0$  for the block and  $E_2 = 10E_0$  for the hollow hemisphere. Contact is computed by the two-half-pass algorithm using the penalty method with  $\varepsilon_0 = 80$  and increasing  $\varepsilon_n^{el} = \varepsilon_t^{el}$  by Eq. (5.3). The friction coefficient is set to  $\mu_{sf} = 0.25$ .

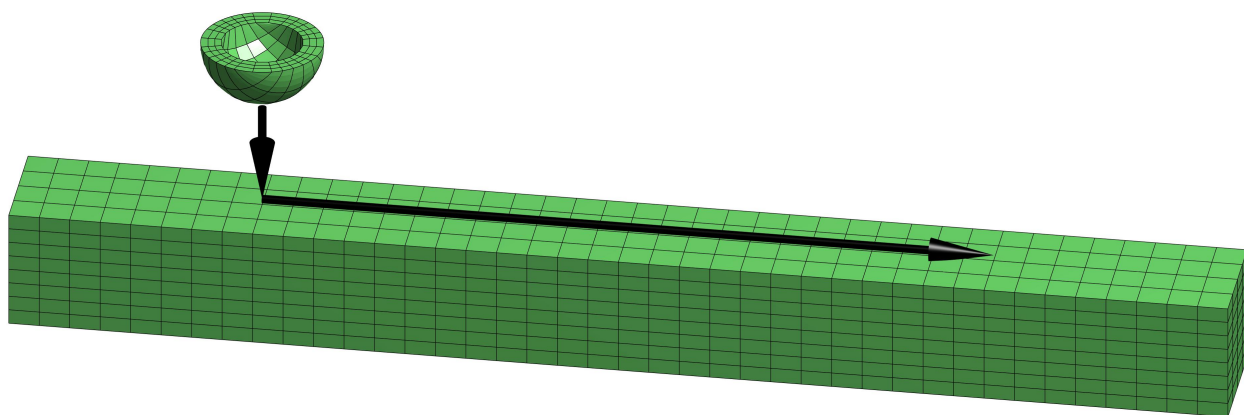


Figure 5.15: Frictional ironing: Problem setup of the hemisphere and the block.

The performance of adaptive local refinement and coarsening using quadratic LR NURBS-enriched finite elements is investigated. For this issue, LR NURBS meshes are compared to uniformly discretized models using quadratic NURBS-enriched finite elements. Local refinement of depth two is applied to investigate the performance and potential of the technique. Fig. 5.16 shows the locally refined and deformed block after the hollow hemisphere is moved downward. The coloring shows the first stress invariant  $I_1 = \text{tr } \boldsymbol{\sigma}/E_0$ . It can be observed that the area of major interest is locally refined while the periphery is left in its coarse fashion. As the surface of the hemisphere is almost entirely in contact with the block the local refinement leads to a uniformly refined hemisphere, see Fig. 5.17.

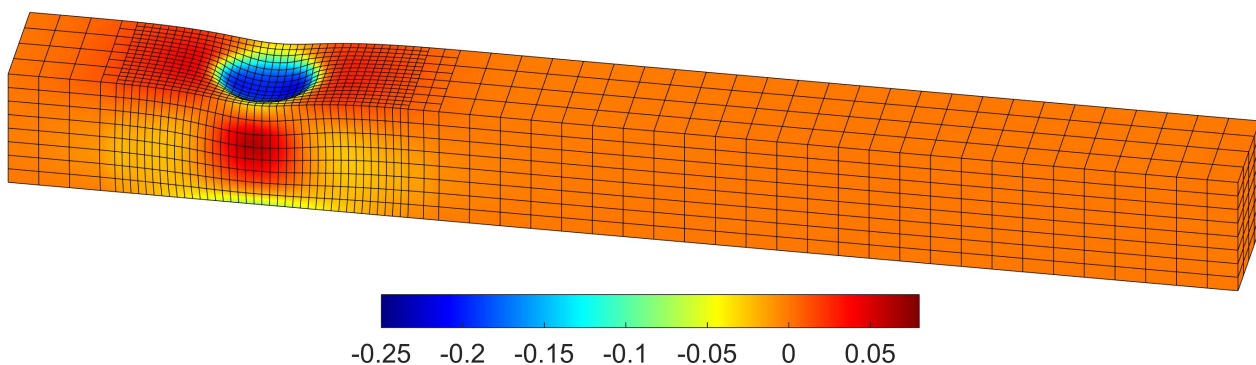


Figure 5.16: Frictional ironing: Deformed, LR NURBS mesh of the block. Refinement of depth two is applied. The coloring shows the first stress invariant  $I_1 = \text{tr } \boldsymbol{\sigma}/E_0$ .

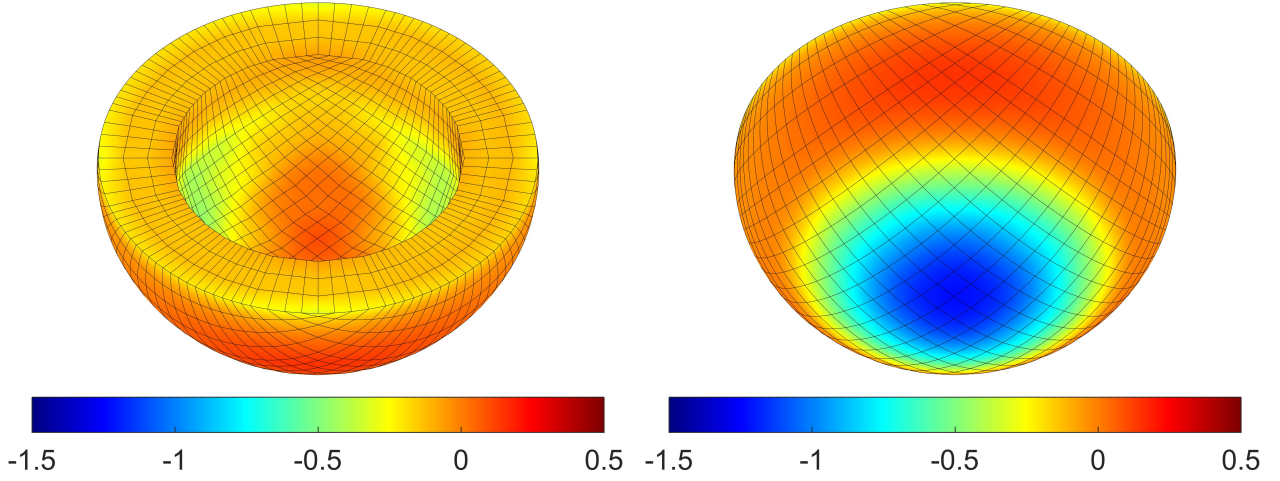


Figure 5.17: Frictional ironing: Refined model of the hollow hemisphere. Top view (left) and bottom view (right). The coloring shows the first stress invariant  $I_1 = \text{tr } \boldsymbol{\sigma} / E_0$ .

The tangential and normal contact forces for LR NURBS and uniform meshes are shown in Fig. 5.18. These are evaluated at the block's contact surface. The contact forces differ slightly from each other for both directions. By first investigating the normal contact force an oscillatory and periodic behavior can be observed. The oscillations can be reduced by further mesh refinement. The trend of the normal contact force of the LR NURBS mesh shows abrupt increases at several points. This is caused by an adaptive local refinement step. The same can be observed by zooming into a coarsening and refinement step in figure of Fig. 5.18 (left).

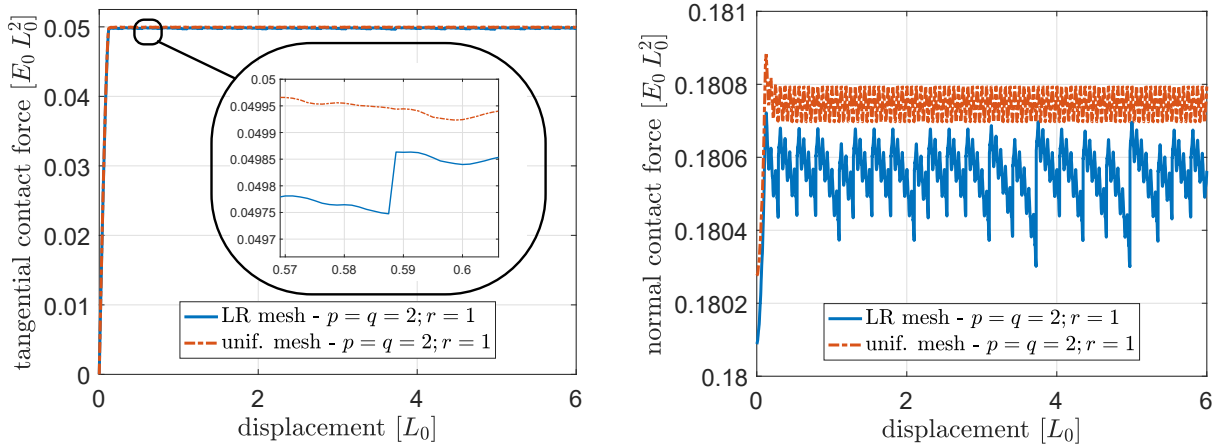


Figure 5.18: Frictional ironing: Tangential (left) and normal (right) contact forces of the LR NURBS and uniform meshes. The LR NURBS mesh uses  $\approx 40\%$  of the dofs in comparison with the uniform mesh.

For further investigations the absolute and relative contact force errors in tangential and normal direction are illustrated in Fig. 5.19. The relative contact force errors are approximately in the range of  $4 \cdot 10^{-4}$  to  $2 \cdot 10^{-3}$ . When entirely sliding is apparent the trend of the errors show a periodic behavior. The errors show a continuous increase which is followed by an abrupt decrease. The errors reflect the influence of the refinement and coarsening technique observed in Fig. 5.18. Comparing the relative contact force error to the results of the previous example we are losing one order of magnitude in accuracy (by comparing quadratic LR NURBS elements). The third dimension of the solids influence the numerical results strongly. For further improvements one should take local error



measures into account. This complex example illustrates that only investigating the contact domain is not satisfying. It is expected that by using cubic LR NURBS-enrichment the error would decrease but this would not reduce the influence of the solid domain.

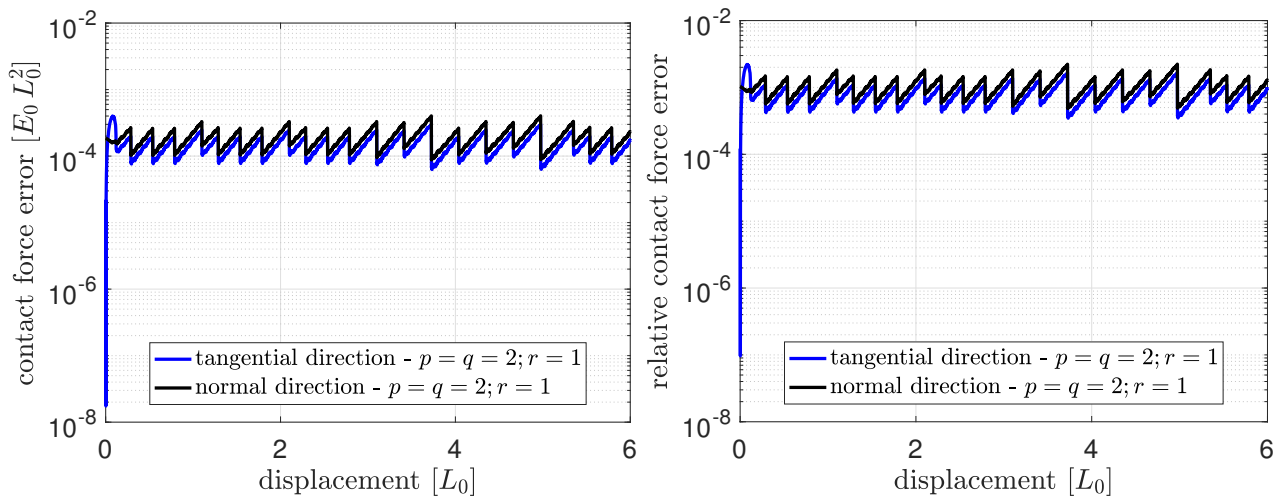


Figure 5.19: Frictional ironing: Absolute (left) and relative (right) error of the tangential and normal contact forces of the LR NURBS mesh w.r.t. the reference solution. The LR NURBS mesh uses  $\approx 40\%$  of the dofs in comparison with the uniform mesh.

Because of a large refined domain the LR NURBS model has still  $\approx 40\%$  of the dofs of the reference model. Reducing the size of the locally refined domain would lead to an increase of the error of the contact forces. Still, the adaptive local refinement and coarsening of LR NURBS-enriched elements show the potential of this procedure.

## 6 Acknowledgments

We are grateful to the German Research Foundation (DFG) for supporting this research through project GSC 111.

## 7 Conclusion

In this work, a novel concept of adaptive local surface refinement using LR NURBS elements in the framework of computational contact is presented. The Bézier extraction of LR NURBS elements by an additional mapping of the Bézier extraction operator is obtained. With this formulation a convenient embedding of LR NURBS elements into general finite element codes is achieved.

The adaptive local refinement and coarsening technique is automatically controlled by the presented refinement indicators. The numerical results show that the geometric approximation error arising from the coarsening is negligible small. The technique is applied to the purely isogeometric membrane formulation and to isogeometrically-enriched solid elements. The numerical examples show the benefit of using LR NURBS elements. Due to the local refinement, the computational cost decreases, while still achieving high accuracy. A good convergence behavior for LR NURBS elements is achieved.

The numerical examples in Sec. 5.1 and Sec. 5.5 show that the extension from LR B-splines to LR NURBS is successful by using truly rational splines. The automatic control of the adaptive local refinement and coarsening technique works robust for frictionless and frictional contact. As

experienced in the examples using quadratic LR NURBS a less accurate results are achieved than in the examples using cubic LR NURBS. This is the result of the error arising from the unrefined elements afar from the contact domain. The cubic LR NURBS elements can capture these domains more accurate due to their higher order interpolation. This issue motivates to incorporate local error measures that indicate elements for refinement. Especially, the computations performed with quadratic LR NURBS-enriched elements show the demand of a local error measure. The refinement depth is prescribed in the presented examples. By using error measures the refinement depth would be set automatically to achieve a desired accuracy.

In this work, only bivariate LR NURBS are considered. Their extension to trivariate LR NURBS would be interesting to allow local refinement of 3D LR NURBS elements. This would be a topic on its own because of the complex structure of trivariate LR NURBS meshes. Ensuring that the resulting LR mesh is linearly independent is not proven yet and is challenging for arbitrary meshline extensions.

## References

- Ainsworth, M. and Oden, J. (1997). A posteriori error estimation in finite element analysis. *Computer Methods in Applied Mechanics and Engineering*, **142**(1-2):1 – 88.
- Benson, D. J., Bazilevs, Y., Hsu, M.-C., and Hughes, T. J. R. (2011). A large deformation, rotation-free, isogeometric shell. *Comp. Methods Appl. Mech. Engrg.*, **200**(13-16):1367–1378.
- Borden, M. J., Scott, M. A., Evans, J. A., and Hughes, T. J. R. (2011). Isogeometric finite element data structures based on Bezier extraction of NURBS. *Int. J. Numer. Meth. Engrg.*, **87**:15–47.
- Bressan, A. (2013). Some properties of LR-splines. *Computer Aided Geometric Design*, **30**(8):778–794.
- Corbett, C. J. and Sauer, R. A. (2014). NURBS-enriched contact finite elements. *Computer Methods in Applied Mechanics and Engineering*, **275**:55 – 75.
- Corbett, C. J. and Sauer, R. A. (2015). Three-dimensional isogeometrically enriched finite elements for frictional contact and mixed-mode debonding. *Comput. Methods Appl. Mech. Engrg.*, **284**:781–806.
- Cottrell, J. A., Hughes, T. J. R., and Bazilevs, Y. (2009). *Isogeometric Analysis*. Wiley.
- Cox, G. (1971). *The Numerical Evaluation of B-Splines*. DNAC. National Physical Laboratory, Division of Numerical Analysis and Computing.
- De Boor, C. (1972). On calculating with B-splines. *Journal of Approximation Theory*, **6**(1):50 – 62.
- De Lorenzis, L., Temizer, I., Wriggers, P., and Zavarise, G. (2011). A large deformation frictional contact formulation using NURBS-based isogeometric analysis. *Int. J. Numer. Meth. Engrg.*, **87**:1278–1300.
- De Lorenzis, L., Wriggers, P., and Zavarise, G. (2012). A mortar formulation for 3D large deformation contact using NURBS-based isogeometric analysis and the augmented Lagrangian method. *Comp. Mech.*, **49**:1–20.
- Demkowicz, L., Oden, J., Rachowicz, W., and Hardy, O. (1989). Toward a universal h-p adaptive finite element strategy, part 1. constrained approximation and data structure. *Computer Methods in Applied Mechanics and Engineering*, **77**(1-2):79 – 112.
- Dokken, T., Lyche, T., and Pettersen, K. F. (2013). Polynomial splines over locally refined box-partitions. *Comp. Aid. Geom. Des.*, **30**(3):331–356.

- Duong, T. X., Roohbakhshan, F., and Sauer, R. A. (2016). A new rotation-free isogeometric thin shell formulation and a corresponding continuity constraint for patch boundaries. *Computer Methods in Applied Mechanics and Engineering*, published online, DOI: <http://dx.doi.org/10.1016/j.cma.2016.04.008>.
- Farin, G. (1992). From conics to NURBS: A tutorial and survey. *IEEE Comput. Graph. Appl.*, **12**(5):78–86.
- Forsey, D. R. and Bartels, R. H. (1988). Hierarchical B-spline refinement. *SIGGRAPH Comput. Graph.*, **22**(4):205–212.
- Hughes, T. J. R., Cottrell, J. A., and Bazilevs, Y. (2005). Isogeometric analysis: CAD, finite elements, NURBS, exact geometry and mesh refinement. *Comp. Meth. Appl. Mech. Engrg.*, **194**:4135–4195.
- Johannessen, K. A., Kumar, M., and Kvamsdal, T. (2015). Divergence-conforming discretization for stokes problem on locally refined meshes using LR B-splines. *Computer Methods in Applied Mechanics and Engineering*, **293**:38 – 70.
- Johannessen, K. A., Kvamsdal, T., and Dokken, T. (2014). Isogeometric analysis using LR B-splines. *Comp. Methods Appl. Mech. Engrg.*, **269**:471–514.
- Kiendl, J., Bletzinger, K.-U., Linhard, J., and Wüchner, R. (2009). Isogeometric shell analysis with Kirchhoff-Love elements. *Comput. Methods Appl. Mech. Engrg.*, **198**:3902–3914.
- Kumar, M., Kvamsdal, T., and Johannessen, K. A. (2015). Simple a posteriori error estimators in adaptive isogeometric analysis. *Computers and Mathematics with Applications*, **70**(7):1555 – 1582. High-Order Finite Element and Isogeometric Methods.
- Laursen, T. A. (2002). *Computational Contact and Impact Mechanics: Fundamentals of modeling interfacial phenomena in nonlinear finite element analysis*. Springer.
- Lu, J. (2011). Isogeometric contact analysis: Geometric basis and formulation for frictionless contact. *Comput. Methods Appl. Mech. Engrg.*, **200**(5-8):726–741.
- Mourrain, B. (2014). On the dimension of spline spaces on planar T-meshes. *Mathematics Of Computation*, **83**(286):847–871.
- Nguyen, D., Rasmuson, A., Thalberg, K., and Björn, I. N. (2014). Numerical modelling of breakage and adhesion of loose fine-particle agglomerates. *Chem. Eng. Sci.*, **116**:91–98.
- Nørtoft, P. and Dokken, T. (2014). *Isogeometric Analysis of Navier-Stokes Flow Using Locally Refinable B-Splines*. Springer International Publishing, Cham.
- Oden, J. T. and Sato, T. (1967). Finite strains and displacements of elastic membranes by the finite element method. *Int. J. Solids Struct.*, **3**(4):471–488.
- Roohbakhshan, F. and Sauer, R. A. (2016). Isogeometric nonlinear shell elements for thin laminated composites based on analytical thickness integration. *Journal of Micromechanics and Molecular Physics*, published online, DOI: [10.1142/S2424913016400105](https://doi.org/10.1142/S2424913016400105).
- Sauer, R. A. and De Lorenzis, L. (2013). A computational contact formulation based on surface potentials. *Computer Methods in Applied Mechanics and Engineering*, **253**:369 – 395.
- Sauer, R. A. and De Lorenzis, L. (2015). An unbiased computational contact formulation for 3D friction. *International Journal for Numerical Methods in Engineering*, **101**(4):251–280.
- Sauer, R. A. and Duong, T. X. (2015). On the theoretical foundations of solid and liquid shells. *Math. Mech. Solids*, published online, DOI: [10.1177/1081286515594656](https://doi.org/10.1177/1081286515594656).

- Sauer, R. A., Duong, T. X., and Corbett, C. J. (2014). A computational formulation for constrained solid and liquid membranes considering isogeometric finite elements. *Comput. Methods Appl. Mech. Engrg.*, **271**:48–68.
- Scott, M. A., Borden, M. J., Verhoosel, C. V., Sederberg, T. W., and Hughes, T. J. R. (2011). Isogeometric finite element data structures based on Bézier extraction of T-splines. *Int. J. Numer. Meth. Engrg.*, **88**(2):126–156.
- Sederberg, T. W., Zheng, J., Bakenov, A., and Nasri, A. (2003). T-splines and T-NURCCs. *ACM Trans. Graph.*, **22**(3):477–484.
- Simo, J. C. and Fox, D. D. (1989). On a stress resultant geometrically exact shell model. Part I: Formulation and optimal parameterization. *Comput. Meth. Appl. Mech. Engrg.*, **72**:267–304.
- Simo, J. C., Fox, D. D., and Rifai, M. S. (1990). On a stress resultant geometrically exact shell model. Part III: Computational aspects of the nonlinear theory. *Comput. Meth. Appl. Mech. Engrg.*, **79**:21–70.
- Temizer, I. and Hesch, C. (2016). Hierarchical NURBS in frictionless contact. *Computer Methods in Applied Mechanics and Engineering*, **299**:161 – 186.
- Temizer, I., Wriggers, P., and Hughes, T. J. R. (2012). Three-dimensional mortar-based frictional contact treatment in isogeometric analysis with NURBS. *Comput. Methods Appl. Mech. Engrg.*, **209-212**:115–128.
- Thomas, D., Scott, M., Evans, J., Tew, K., and Evans, E. (2015). Bézier projection: A unified approach for local projection and quadrature-free refinement and coarsening of NURBS and T-splines with particular application to isogeometric design and analysis. *Computer Methods in Applied Mechanics and Engineering*, **284**(0):55 – 105.
- Wriggers, P. (2006). *Computational Contact Mechanics*. Springer, 2<sup>nd</sup> edition.
- Wriggers, P. (2008). *Nonlinear Finite Element Methods*. Springer.
- Zienkiewicz, O. C., Taylor, R. L., and Zhu, J. Z. (2005). *The Finite Element Method: Its basis and fundamentals*. Butterworth-Heinemann, 6<sup>th</sup> edition.